

# Exclusive $\eta$ production in proton-proton collisions at energies available at the GSI Facility for Antiproton and Ion Research

Piotr Lebiedowicz<sup>1,\*</sup>

<sup>1</sup>*Institute of Nuclear Physics Polish Academy of Sciences, Radzikowskiego 152, PL-31342 Kraków, Poland*

The cross sections for the  $pp \rightarrow pp\eta$  reaction are evaluated at energies relevant for the HADES, PANDA, and SIS100 experiments at GSI-FAIR. Consideration includes the  $\eta$ -bremsstrahlung mechanism involving intermediate proton exchange via the  $\pi^0$ ,  $\eta$ ,  $\rho^0$ , and  $\omega$  exchanges and the mechanism involving the nucleon resonances  $N(1535)$ ,  $N(1650)$ ,  $N(1710)$ , and  $N(1880)$  excited via the pseudoscalar- and/or vector-meson exchanges, depending on the model. The role of the  $\omega\omega$ - and  $\rho^0\rho^0$ -fusion processes with the reggeized vector-meson exchanges is also discussed. The calculation is done in an effective Lagrangian approach. To determine the parameters of the model, the  $\gamma p \rightarrow \eta p$  and  $\pi^- p \rightarrow \eta n$  reactions are studied and the results are then compared with the Crystal Ball and CLAS data. For the  $pp \rightarrow pp\eta$  reaction, the model results are compared with the energy dependence of the cross section measured far from the threshold and with the differential distributions  $d\sigma/d\cos\theta_\eta$  and  $d\sigma/dp_\eta$  measured by the DISTO Collaboration. The comparison shows that the  $N(1535)$  resonance is the dominant contribution and that other contributions are also important due to interference effects. Assuming that the  $\rho$  exchange is the dominant resonant excitation process, the model is able to describe the available data, e.g., it reproduces the shape of the angular distributions measured by the DISTO Collaboration. Predictions are given for the HADES experiment at center-of-mass energy of  $\sqrt{s} = 3.46$  GeV, which can be verified in the near future, and for planned PANDA and SIS100 experiments at higher energies.

## I. INTRODUCTION

The production of light pseudoscalar  $\eta$  and  $\eta'(958)$  mesons with quantum numbers  $I^G(J^{PC}) = 0^+(0^{-+})$  is very interesting. In particular, the production mechanism of  $\eta$  has been discussed in a number of papers. However, it still requires further theoretical and experimental investigation. For a nice review of physics with the  $\eta$  and  $\eta'$  mesons see [1]. The exclusive production of the  $\eta$  meson near the kinematical threshold in nucleon-nucleon collisions was discussed in [2–22] and in [23].

Most calculations of  $\eta$  production in nucleon-nucleon collisions indicate a dominant role of resonances, in particular the  $N(1535)$  resonance formed by the exchange of virtual mesons. Several phenomenological models, although based on different assumptions about the excitation mechanism of nucleon resonances, describe the  $pp \rightarrow pp\eta$  near-threshold data quite well. For example, in [2, 3, 6, 7] the  $\rho$  exchange is found to contribute much more to  $N(1535)$  than the  $\pi$  or  $\eta$  exchanges. The importance of the  $\omega$  exchange was emphasized in [4], while some importance of the two- $\pi$  exchange (simulated by a  $\sigma$  exchange) was found in [5]. The one-meson exchange model developed by Fäldt and Wilkin [9], which assumes a dominant excitation of the  $N(1535)$  resonance by the exchange of the  $\rho$  meson with destructive  $\rho/\pi$  interference, reproduces the near-threshold data. There it was found that the contribution of the  $\rho$  exchange is larger than that of the  $\pi$  exchange. An alternative model discussed in [10] explains that the relative importance of the different meson exchange (rescattering) contribu-

tions is strongly influenced by the nucleon-nucleon initial state interaction (ISI) effect. It was shown that the  $\pi$  and  $\rho$  exchanges have almost the same strength and give comparable cross sections before the ISI effect is included. After including the ISI effect, the  $\pi$  exchange plays the dominant role. However, the contributions of the other terms ( $\rho$ ,  $\eta$ ,  $\sigma$ ) and the direct term are still significant due to interference effects with the  $\pi$  term. In the model presented in [15], the  $\eta$  exchange contribution is comparable to the leading  $\pi$  exchange term, and due to the phenomenological final state interaction there is no need to introduce other meson exchanges. In recent calculations [18–20], it was shown that a good agreement with the near-threshold data can also be obtained by excitation of the nucleon resonances by different exchange mesons, including nucleonic and mesonic currents and possible interference effects. The interference between several amplitudes influences the behavior of differential cross-section distributions, which is a way to distinguish different models by comparison with experiment. In [15, 18, 19] it was suggested that the initial ( $NN$  ISI) and final state ( $NN$  and  $\eta N$  FSI) interactions are essential to obtain the shape and size of the total cross section. In [11, 19] it was found that terms corresponding to the excitation of the  $N(1535)$  resonance via the  $\pi$ -exchange process dominate the cross section. In [20] Nakayama and co-authors developed the model based on a combined analysis of  $\eta$  meson hadro- and photo-production off nucleons, and discussed two scenarios for the  $NN \rightarrow NN\eta$  reactions that differ in the dynamical content. In the first scenario, the  $S_{11}(1535 + 1650)$  term dominates over the  $D_{13}(1520 + 1700)$  resonance contribution to the cross section, while in the second case the  $D_{13}$  resonance excitation is the dominant production mechanism, especially at lower energies. The

\* Piotr.Lebiedowicz@ifj.edu.pl

quality of the near-threshold experimental data does not allow one to unambiguously distinguish different dynamical contributions. It still remains to be verified whether the dominance of the  $D_{13}$  contribution discussed in [20] is indeed true. The predictions available in the literature are still not conclusive. It is clear that high-precision data on the  $pp \rightarrow pp\eta$  reaction are needed to draw firm conclusions about its dynamics.

The present study estimates the total and differential cross sections for the  $pp \rightarrow pp\eta$  reaction at higher energies. The emphasis is on the production mechanism of the  $\eta$  meson in the kinematic region where existing data are scarce and of relatively low accuracy. The results presented in this work will be compared with data obtained by the DISTO Collaboration [24] and the HADES Collaboration [25–27]. Recently, efforts have been made to complement and extend cross-section database, in particular at the GSI facilities in Darmstadt (Germany). In February 2022, proton-proton reactions at 4.5 GeV beam kinetic energy (center-of-mass energy  $\sqrt{s} = 3.46$  GeV) were measured by the HADES Collaboration; see e.g. [28, 29]. They may provide new and valuable information to test theoretical models for the exclusive production of light mesons, and notably in a kinematic region that has been poorly studied so far. In Ref. [30], the exclusive production of  $f_1(1285)$  meson at energies relevant for the HADES and PANDA experiments at GSI-FAIR was discussed. There, the vector-meson fusion mechanism was investigated. It is worth mentioning, that at higher energies the diffractive mechanism described by Reggeon and Pomeron exchanges, as well as the fusion mechanism of corresponding Regge exchanges, begin to play an important role. Additional measurements, including those in the energy range of SIS100 at GSI [31] ( $\sqrt{s} \approx 8$  GeV), are needed to explore the size and significance of individual contributions and would therefore be very welcome.

Diffractive exclusive production of  $\eta$  and  $\eta'$  mesons in proton-proton collisions at high energies was discussed in [32, 33], more recently in [34, 35] within the tensor-Pomeron approach [36], and in [37, 38] in the Sakai-Sugimoto model. Two-gluon component of the  $\eta$  and  $\eta'$  mesons to leading-twist accuracy was discussed in [39]. For a study of gluon dynamics in low-energy QCD and a discussion of the connection of light pseudoscalar mesons to anomalous glue, interested readers are referred to [40]. Hopefully, new experimental data for the  $pp \rightarrow pp\eta$  reaction will be accurate enough to learn

more about short-range hadron dynamics.

For a review of  $\eta$  and  $\eta'$  photo- and hadro-production on nucleons and on nuclei see e.g. [23]. The  $\eta$  photoproduction  $\gamma p \rightarrow \eta p$  was measured by several experimental groups, e.g., MIT [41], DESY [42], Dewire *et al.* [43], CLAS [44, 45], CBELSA/TAPS [46], and MAMI [47]. In Refs. [46, 47] the  $\eta$  mesons were observed in their neutral decay modes. Recently, the CLAS Collaboration [48] measured the photoproduction of  $\eta$  mesons in their dominant charged decay mode  $\eta \rightarrow \pi^+ \pi^- \pi^0$ . Several approaches were developed to describe the experimental data available at that time; see, e.g., [49], [20], a chiral quark model [50], JPAC [51],  $\eta$ -MAID 2018 [52, 53]. There, the  $t$ -channel  $\rho$  and  $\omega$  exchange (either Regge trajectories or meson exchanges) is the dominant reaction mechanism for the small- $t$  behavior of the cross section, i.e., in the forward scattering region. The CLAS data on  $\eta$  photoproduction [48] give access to the energy range beyond the nucleon resonance region and thus allow a comparison with the Regge-based model predictions.

The paper is organized as follows. In Sec. II, the model for the  $\eta$  production in proton-proton collisions is briefly described. Section III presents the numerical results of the calculations for the total and differential cross sections of the  $pp \rightarrow pp\eta$  reaction. The numerical results for three models are presented and discussed for energies far from the threshold relevant for upcoming and planned measurements. Section IV summarizes my conclusions. In Appendixes A and B, the  $\pi^- p \rightarrow \eta n$  and  $\gamma p \rightarrow \eta p$  reactions which are helpful in determining and validating some model parameters used for the  $pp \rightarrow pp\eta$  reaction are discussed. Appendix C focuses on  $\rho NN^*$  coupling constants.

## II. FORMALISM

The exclusive production of the pseudoscalar  $\eta$  meson in proton-proton collisions is the subject of this study:

$$p(p_a, \lambda_a) + p(p_b, \lambda_b) \rightarrow p(p_1, \lambda_1) + p(p_2, \lambda_2) + \eta(k), \quad (2.1)$$

where  $p_{a,b}$ ,  $p_{1,2}$ , and  $\lambda_{a,b}$ ,  $\lambda_{1,2} = \pm \frac{1}{2}$  denote the four-momenta and helicities of the nucleons, respectively, and  $k$  denotes the four-momentum of the  $\eta$  meson. The cross section is as follows:

$$\begin{aligned} \sigma(pp \rightarrow pp\eta) = & \frac{1}{2} \frac{1}{2\sqrt{s(s-4m_p^2)}} \int \frac{d^3 k}{(2\pi)^3 2k^0} \frac{d^3 p_1}{(2\pi)^3 2p_1^0} \frac{d^3 p_2}{(2\pi)^3 2p_2^0} (2\pi)^4 \delta^{(4)}(p_1 + p_2 + k - p_a - p_b) \\ & \times \frac{1}{4} \sum_{\text{spins}} |\mathcal{M}_{pp \rightarrow pp\eta}|^2, \end{aligned} \quad (2.2)$$

including a statistics factor  $\frac{1}{2}$  due to identical particles appear in the final state.

The amplitude reads

$$\mathcal{M}_{pp \rightarrow pp\eta} = \mathcal{M}_{pp \rightarrow pp\eta}(p_1, p_2) - \mathcal{M}_{pp \rightarrow pp\eta}(p_2, p_1). \quad (2.3)$$

The relative minus sign here is due to the Fermi statistics, which requires the amplitude to be antisymmetric under interchange of the two final protons.

In the calculations, the complete amplitude  $\mathcal{M}_{pp \rightarrow pp\eta}$  is considered as a sum due to the bremsstrahlung (BS) and the  $VV$  fusion processes ( $VV = \rho^0 \rho^0, \omega \omega$ ) con-

tributing to  $pp \rightarrow pp\eta$ :

$$\mathcal{M}_{pp \rightarrow pp\eta} = \mathcal{M}_{pp \rightarrow pp\eta}^{(BS)} + \mathcal{M}_{pp \rightarrow pp\eta}^{(VV)}. \quad (2.4)$$

Details will be given when discussing the production mechanisms below.

### A. The $\eta$ -bremsstrahlung mechanism

The  $\eta$ -production mechanism via an intermediate nucleon and nucleon resonances is shown in Fig. 1.

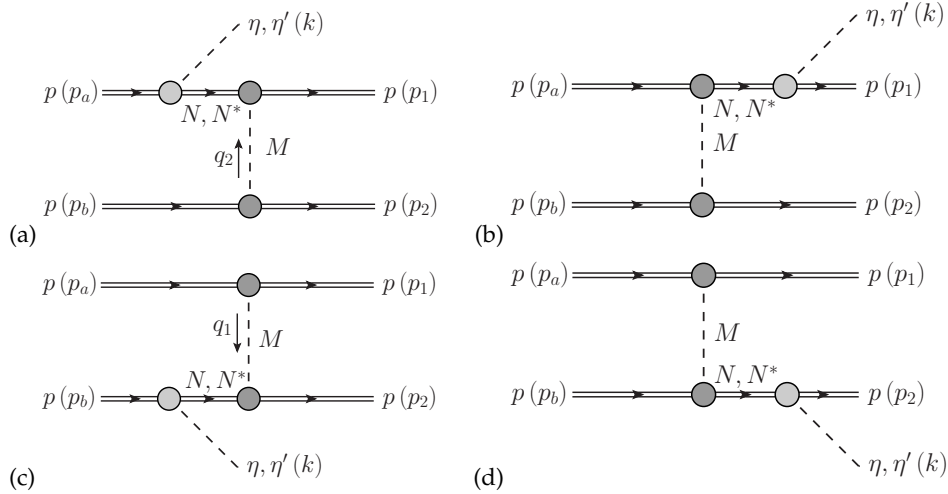


FIG. 1. The diagrams for the  $\eta$  (or  $\eta'$ ) production with an intermediate nucleon ( $N$ ) or a nucleon resonance ( $N^*$ ).  $M$  stands for a single meson exchange. The diagrams (a), (c) and (b), (d) are usually called pre- and post-emission diagrams, respectively. There are also the diagrams corresponding to the interchange of the two final protons  $p(p_1) \leftrightarrow p(p_2)$ . These are not shown here.

The generic amplitude for the  $pp \rightarrow pp\eta$  reaction reads

$$\mathcal{M}_{pp \rightarrow pp\eta}^{(BS)} = \sum_{i=N, N^*} \sum_{j=M} \left( \mathcal{M}^{(a)ij} + \mathcal{M}^{(b)ij} + \mathcal{M}^{(c)ij} + \mathcal{M}^{(d)ij} \right). \quad (2.5)$$

The amplitudes for the diagrams corresponding to the exchange of protons  $p(p_1) \leftrightarrow p(p_2)$  are also taken into account with appropriate kinematics and with a negative sign.

For the  $\eta$ -bremsstrahlung mechanism with the intermediate proton all set of the diagrams is shown in Fig. 1 with the exchange of virtual mesons  $M = \pi^0, \eta, \rho^0, \omega$ . In the present analysis, the processes with the  $\sigma, \eta', a_0$  and exchanges were neglected due to small or/and rather poorly known relevant  $MNN$  and  $MNN^*$  coupling constants. In addition, these exchanges are expected to be small relative to the  $\pi^0$  exchange because of the heavier mass occurring in the meson propagator. The analy-

sis includes the mechanism involving the  $N^*$  resonances excited through the exchange of a single meson, limiting one to the so-called post-emission diagrams, i.e., the diagrams (b) and (d) of Fig. 1. In these diagrams, the  $\eta$  meson is formed through the decay of the  $N^*$  resonance. Pre-emission diagrams give only a negligible contribution because of kinematic reasons. This is a reasonable simplification, since the analysis of the  $\pi^- p \rightarrow \eta n$  and  $\gamma p \rightarrow \eta p$  processes indicates that the  $u$ -channel  $N^*$ -exchange contributions are very small; see the discussion in Appendixes A and B.

As an example, the amplitude for the  $pp \rightarrow pp\eta$  reaction with excitation of the intermediate spin-1/2 nucleon resonance after the  $\pi^0$ -meson exchange [the post-emission diagram shown in Fig. 1 (b)] is written as

$$\mathcal{M}_{\lambda_a \lambda_b \rightarrow \lambda_1 \lambda_2 \eta}^{(b)N_{1/2}^* \pi^0}(s, t_2) = (-i) \bar{u}(p_1, \lambda_1) i\Gamma^{(\eta NN_{1/2}^*)}(p_1, p_{1f}) iP^{(N_{1/2}^*)}(p_{1f}^2) i\Gamma^{(\pi NN_{1/2}^*)}(p_{1f}, p_a) u(p_a, \lambda_a) \times i\Delta^{(\pi)}(q_2) \bar{u}(p_2, \lambda_2) i\Gamma^{(\pi NN)}(p_2, p_b) u(p_b, \lambda_b), \quad (2.6)$$

where  $p_{1f} = p_a + q_2 = p_1 + k$ ,  $q_2 = p_b - p_2$ ,  $t_2 = q_2^2$ . The effective vertices  $\pi NN$ ,  $\eta NN$ ,  $\pi NN^*$ ,  $\eta NN^*$  are obtained from the interaction Lagrangians given in Appendix A. The absolute value of the coupling constants  $MNN^*$  can be determined by using the partial decay widths of the resonances with the compilation of Particle Data Group (PDG) data; see Table II in Appendix A.

Each vertex in (2.6) incorporates a phenomenological cutoff function

$$F_{\pi NN^*}(q^2, p_N^2, p_{N^*}^2) = F_\pi(q^2) F_B(p_N^2) F_B(p_{N^*}^2), \quad (2.7)$$

where  $q$  denotes the four-momentum of the intermediate pion  $\pi^0$ , while  $p_N$  and  $p_{N^*}$  are the four-momenta of the two baryons. For the form factor  $F_B(p^2)$  with  $B = N, N_{1/2}^*$  one proceeds as in (A20),

$$F_\pi(q^2) = \frac{\Lambda_{\pi NN^*}^2 - m_\pi^2}{\Lambda_{\pi NN^*}^2 - q^2}. \quad (2.8)$$

In the calculations the cutoff parameter  $\Lambda_{\pi NN^*} = 1.2$  GeV for each  $N^*$  resonance is used. Furthermore, in the  $\pi NN$  vertex, the monopole form factor is taken:

$$F_{\pi NN}(q^2) = \frac{\Lambda_{\pi NN}^2 - m_\pi^2}{\Lambda_{\pi NN}^2 - q^2}. \quad (2.9)$$

Here  $\Lambda_{\pi NN} = 1.0$  GeV. Analogously, the  $\eta$ -exchange amplitude is derived, but with the parameters  $\Lambda_{\eta NN} = 1.0$  GeV and  $\Lambda_{\eta NN^*} = 1.2$  GeV.

The amplitude with the  $\rho^0$ -meson exchange, corresponding to Fig. 1 (b), is obtained from (2.6) by making the replacements:

$$\begin{aligned} \Delta^{(\pi)}(q_2) &\rightarrow \Delta_{\mu\nu}^{(\rho)}(q_2), \\ \Gamma^{(\pi NN_{1/2}^*)}(p_{1f}, p_a) &\rightarrow \Gamma^{(\rho NN_{1/2}^*)\mu}(p_{1f}, p_a), \\ \Gamma^{(\pi NN)}(p_2, p_b) &\rightarrow \Gamma^{(\rho NN)\nu}(p_2, p_b). \end{aligned} \quad (2.10)$$

The vector-meson-proton vertex is given in (2.18) and the effective coupling for  $\rho NN_{1/2}^*$  is discuss in Appendix C.

In the calculation of the amplitudes the propagators for various baryons and mesons are needed. For nucleon and nucleon resonances see Eqs. (A13)–(A15). For pseudoscalar mesons one has  $\Delta^{(\pi, \eta)}(q) = (q^2 - m_{\pi, \eta}^2)^{-1}$ . The propagators for  $\rho$  and  $\omega$  mesons are given by Eq. (2.21). The amplitudes with vector-meson exchanges were multiplied by a purely phenomenological suppression function in order to ensure a correct energy dependence:

$$f_{\text{sup}}(s) = \exp \left( -\frac{s - s_{\text{thr}}}{\Lambda_{\text{sup}}^2} \right) \quad (2.11)$$

with  $s_{\text{thr}} = (2m_p + m_\eta)^2$  and  $\Lambda_{\text{sup}} = 4$  GeV (unless stated otherwise).

Before presenting the calculated results for the  $pp \rightarrow pp\eta$  reaction, it is worth discuss the possible role of the initial state interaction (ISI) and final state interaction (FSI) between the nucleons, i.e., the effects before and after the  $\eta$  creation. The ISI and/or FSI effects were discussed in more detail in [10, 15, 18, 19, 54–57]. The  $NN$  FSI effect is significant for small excess energies  $Q_{\text{exc}} = \sqrt{s} - \sqrt{s_{\text{thr}}}$ . In the present case, for the  $\eta$  production at  $\sqrt{s} \geq 3.46$  GeV one has  $Q_{\text{exc}} > 625$  MeV and the  $NN$  FSI effect can be safely neglected. As mentioned in [10] for the  $\eta$  production at near-threshold energies, for the model calculation without  $NN$  ISI the dominant contributions come from  $\pi$  and  $\rho$  exchanges, both being of comparable magnitude. There, however, the ISI reduces the contribution of  $\rho$  exchange much more than that of  $\pi$  exchange, leaving  $\pi$  exchange as the only dominant production mechanism. The author of Ref. [19] predicted that, close to the threshold, the full ( $NN$  and  $\eta N$ ) FSI effect can have similar strength as  $NN$  ISI, but increase the cross section. It is known that ISI also plays an important role in the HADES and PANDA energy range; see, e.g., Refs. [58, 59]. Previous studies have shown that both ISI and FSI effects are not universal, but depend, among other factors, on the considered reaction and the concrete meson production mechanism. Further study on the consistent treatment of these effects in the considered approach, including their potential impact on the final results (both on the energy dependence of the cross section and on the shape of the distributions) is postponed for future work.

## B. The $VV$ -fusion mechanism

The  $VV$ -fusion mechanism ( $VV$  stands for  $\rho^0\rho^0$  or  $\omega\omega$ ) is represented by the diagrams in Fig. 2. The kinematic variables are

$$\begin{aligned} q_1 &= p_a - p_1, & q_2 &= p_b - p_2, & k &= q_1 + q_2, \\ t_1 &= q_1^2, & t_2 &= q_2^2, & m_\eta^2 &= k^2, \\ s &= (p_a + p_b)^2 = (p_1 + p_2 + k)^2, \\ s_1 &= (p_a + q_2)^2 = (p_1 + k)^2, \\ s_2 &= (p_b + q_1)^2 = (p_2 + k)^2. \end{aligned} \quad (2.12)$$

For the kinematics see, e.g., Appendix D of [34].

The  $VV$ -fusion amplitude ( $VV = \rho^0\rho^0, \omega\omega$ ) is

$$\mathcal{M}_{pp \rightarrow pp\eta}^{(VV)} = \mathcal{M}_{pp \rightarrow pp\eta}^{(\rho\rho \text{ fusion})} + \mathcal{M}_{pp \rightarrow pp\eta}^{(\omega\omega \text{ fusion})}, \quad (2.13)$$

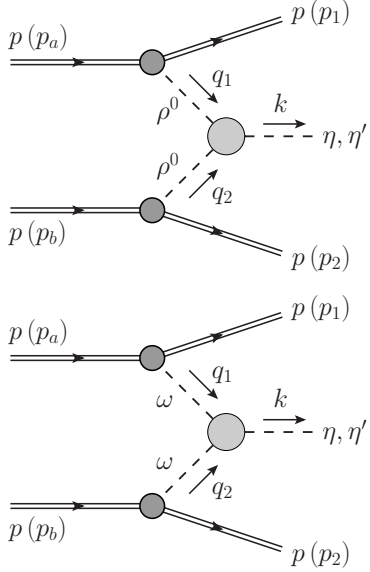


FIG. 2. The  $\rho\rho$ - and  $\omega\omega$ -fusion mechanism for  $\eta$  production in proton-proton collisions. In addition there are the diagrams corresponding to the interchange  $p(p_1) \leftrightarrow p(p_2)$ .

where one has<sup>1</sup>

$$\begin{aligned} \mathcal{M}_{\lambda_a \lambda_b \rightarrow \lambda_1 \lambda_2 \eta}^{(VV \text{ fusion})} = & (-i) \bar{u}(p_1, \lambda_1) i\Gamma_{\mu_1}^{(Vpp)}(p_1, p_a) u(p_a, \lambda_a) \\ & \times i\tilde{\Delta}^{(V)} \nu_1 \nu_1(s_1, t_1) i\Gamma_{\nu_1 \nu_2}^{(VV\eta)}(q_1, q_2) \\ & \times i\tilde{\Delta}^{(V)} \nu_2 \mu_2(s_2, t_2) \\ & \times \bar{u}(p_2, \lambda_2) i\Gamma_{\mu_2}^{(Vpp)}(p_2, p_b) u(p_b, \lambda_b) \\ & - [p_1, \lambda_1 \leftrightarrow p_2, \lambda_2]. \end{aligned} \quad (2.14)$$

Here, omitting the Lorentz indices,  $\Gamma^{(VV\eta)}$  and  $\Gamma^{(Vpp)}$  are the  $VV\eta$  and  $Vpp$  vertex functions, respectively, and  $\tilde{\Delta}^{(V)}$  is the propagator for the reggeized vector meson  $V$ . I now discuss all these quantities in turn.

The  $VV\eta$  vertices are derived from an effective Lagrangians [18, 60]

$$\begin{aligned} \mathcal{L}_{\rho\rho\eta} &= \frac{g_{\rho\rho\eta}}{2m_\rho} \epsilon_{\mu\nu\alpha\beta} (\partial^\mu \Phi_\rho^\nu \partial^\alpha \Phi_\rho^\beta) \Phi_\eta, \\ \mathcal{L}_{\omega\omega\eta} &= \frac{g_{\omega\omega\eta}}{2m_\omega} \epsilon_{\mu\nu\alpha\beta} (\partial^\mu \Phi_\omega^\nu \partial^\alpha \Phi_\omega^\beta) \Phi_\eta, \end{aligned} \quad (2.15)$$

where  $g_{VV\eta}$  are dimensionless coupling constants,  $\Phi$  are the meson fields (a bold face letter stands for an isovector). For the Levi-Civita symbol the convention  $\epsilon_{0123} = 1$  is used. The  $VV\eta$  vertex, including form factor, with  $q_1, \mu$  and  $q_2, \nu$  the momenta and vector indices

of the incoming  $V$  mesons, is then given by

$$i\Gamma_{\mu\nu}^{(VV\eta)}(q_1, q_2) = i \frac{g_{VV\eta}}{2m_V} \epsilon_{\mu\nu\alpha\beta} q_1^\alpha q_2^\beta F^{(VV\eta)}(q_1^2, q_2^2, k^2). \quad (2.16)$$

According to the procedure for determining the coupling constant  $g_{VV\eta}$  from the radiative meson decays  $V \rightarrow \eta\gamma$  in conjunction with the VMD assumption (see Appendix B), the form factor  $F^{(VV\eta)}$  is normalized to unity when one vector meson is on-mass shell and the other one becomes massless, i.e.,  $F^{(VV\eta)}(0, m_V^2, m_\eta^2) = 1$ . One can use

$$F^{(VV\eta)}(t_1, t_2, m_\eta^2) = \frac{\Lambda_V^2}{\Lambda_V^2 - t_1} \frac{\Lambda_V^2 - m_V^2}{\Lambda_V^2 - t_2} \quad (2.17)$$

and  $\Lambda_V = \Lambda_{V, \text{mon}} = 1.2$  GeV motivated by analysis of the  $\gamma p \rightarrow \eta p$  reaction in Appendix B.

The vector-meson-proton vertex is

$$\begin{aligned} i\Gamma_\mu^{(Vpp)}(p', p) = & -ig_{Vpp} F_{VNN}(t) \\ & \times \left[ \gamma_\mu - i \frac{\kappa_V}{2m_p} \sigma_{\mu\nu} (p - p')^\nu \right] \end{aligned} \quad (2.18)$$

where  $\kappa_V = f_{VNN}/g_{VNN}$  is the tensor-to-vector coupling ratio with the following values for coupling constants:

$$g_{\rho pp} = 3.0, \quad \kappa_\rho = 6.1, \quad g_{\omega pp} = 9.0, \quad \kappa_\omega = 0; \quad (2.19)$$

see also the discussion in [30]. The form factor  $F_{VNN}(t)$  in (2.18), describing the  $t$  dependence of the  $V$ -proton coupling, can be parametrized as

$$F_{VNN}(t) = \frac{\Lambda_{VNN}^2 - m_V^2}{\Lambda_{VNN}^2 - t}, \quad (2.20)$$

where  $\Lambda_{VNN} > m_V$  and  $t < 0$ . Here,  $\Lambda_{VNN} = 1.4$  GeV was used for both  $\rho^0$ - and  $\omega$ -proton coupling.<sup>2</sup>

The standard form of the vector-meson propagator is given, e.g., in (3.2) of [36]:

$$\begin{aligned} i\Delta_{\mu\nu}^{(V)}(q) = & i \left( -g_{\mu\nu} + \frac{q_\mu q_\nu}{q^2 + i\epsilon} \right) \Delta_T^{(V)}(q^2) \\ & - i \frac{q_\mu q_\nu}{q^2 + i\epsilon} \Delta_L^{(V)}(q^2). \end{aligned} \quad (2.21)$$

Here  $\Delta_T^{(V)}(t) = (t - m_V^2)^{-1}$ . With the relations for the  $VV\eta$  vertex (2.16),

$$\Gamma_{\mu\nu}^{(VV\eta)}(q_1, q_2) q_1^\mu = 0, \quad \Gamma_{\mu\nu}^{(VV\eta)}(q_1, q_2) q_2^\nu = 0, \quad (2.22)$$

<sup>1</sup> The last term in (2.14), corresponding to the exchange of protons  $p(p_1, \lambda_1) \leftrightarrow p(p_2, \lambda_2)$ , is calculated in a similar way as the first term but with appropriate kinematics and with a negative sign.

<sup>2</sup> From the Bonn potential model [61]  $\Lambda_{\rho NN} = 1.4$  GeV and  $\Lambda_{\omega NN} = 1.5$  GeV are required for a fit to  $NN$  scattering data; see Table 4 of [61].

the terms  $\propto q_\mu q_\nu$  in (2.21) do not contribute in (2.14). According to the arguments presented in [30] the reggeized vector meson propagator  $\tilde{\Delta}_{\mu\nu}^{(V)}(s_i, t_i)$  is used in (2.14). It is obtained from (2.21) with the replacement

$$\begin{aligned} \Delta_T^{(V)}(t_i) &\rightarrow \tilde{\Delta}_T^{(V)}(s_i, t_i), \\ \tilde{\Delta}_T^{(V)}(s_i, t_i) &= \Delta_T^{(V)}(t_i) \left( \exp(i\phi(s_i)) \frac{s_i}{s_{\text{thr}}} \right)^{\alpha_V(t_i)-1}, \end{aligned} \quad (2.23)$$

where

$$\phi(s_i) = \frac{\pi}{2} \exp\left(\frac{s_{\text{thr}} - s_i}{s_{\text{thr}}}\right) - \frac{\pi}{2}, \quad (2.24)$$

$$s_{\text{thr}} = (m_p + m_\eta)^2, \quad (2.25)$$

and the non-linear form of the vector-Regge trajectory, the so-called “square-root” trajectory [62],

$$\alpha_V(t) = \alpha_V(0) + \gamma \left( \sqrt{T_V} - \sqrt{T_V - t} \right). \quad (2.26)$$

The parameters are fixed to be  $\alpha_\rho(0) = 0.55$ ,  $\gamma = 3.65 \text{ GeV}^{-1}$ ,  $\sqrt{T_\rho} = 2.46 \text{ GeV}$ ; see Table I of [62]. The intercept of the  $\rho$  trajectory is rather well known  $\alpha_\rho(0) \approx 0.55$ ; see [62] and references therein. Since  $m_\omega > m_\rho$ , the intercepts of  $\omega$  and  $\rho$  trajectories should satisfy  $\alpha_\omega(0) < \alpha_\rho(0)$ . Note that  $\alpha_V(0) \lesssim 0.5$  in Refs. [51, 52]. Therefore, for the  $\omega$  trajectory,  $\alpha_\omega(0) = 0.5$ , and  $\sqrt{T_\omega} = \sqrt{T_\rho}$  in (2.26), are used.

Other fusion mechanisms, such as  $\omega\phi(\phi\omega) \rightarrow \eta$  and  $\phi\phi \rightarrow \eta$ , can be neglected due to much smaller coupling constants and the heavier mass of  $\phi$  occurring in the propagator; see the discussion in [60, 63]. There can be also the  $a_0\pi^0(\pi^0a_0) \rightarrow \eta$  fusion processes discussed in [11]. In the present work, these contributions are neglected due to the uncertainty in the off-shell form factor and rather poorly known coupling constants. Note that in [11, 60] these processes were estimated to be small contributions.

### III. RESULTS

This section presents the numerical results of the calculations and the comparison of these with existing experimental data. It should be stressed that the results presented here for the  $pp \rightarrow pp\eta$  reaction may not represent optimal solutions within the present approach. The results should be considered as examples of the possible features that can be obtained within a rather simplified model. The model parameters are obtained by fitting the model results to the available data for the  $\gamma p \rightarrow \eta p$  and  $\pi^- p \rightarrow \eta n$  reactions and by matching the experimental radiative decay widths, as explained in Appendices A, B, and C.

In the following, theoretical predictions for three models are presented. They differ in the way the resonances are excited (the number and type of exchanged mesons) and may differ in the type of couplings and their parameter values. Model 1 and model 2 assume the dominance of the  $\rho$  exchange (there is no exchange of pseudoscalar mesons). Model 1 uses the pseudoscalar (PS) type  $g_{\eta NN^*}$  couplings (A5), (A6) for all included  $N^*$  resonances, i.e., for  $N(1535)$ ,  $N(1655)$ ,  $N(1710)$  and  $N(1880)$ . Model 2 is the same as model 1 except that for the even parity resonances  $N(1710)$ , and  $N(1880)$  the pseudovector (PV) type  $g_{\eta NN^*}$  couplings (A7), (A8) were used. In both model 1 and model 2 the  $g_{\eta NN^*}$  coupling constants were taken from Table II in Appendix A, assuming the upper value for  $N(1710)$ . For model 1, the  $\rho NN^*$  coupling constants are as follows:  $g_{\rho NN(1535)} = 5.0$ ,  $g_{\rho NN(1650)} = 1.5$ ,  $g_{\rho NN(1710)} = 0.4$ ,  $g_{\rho NN(1880)} = 1.5$ , and a universal value of  $\Lambda_\rho = 1.2 \text{ GeV}$  for all resonances. Model 2, on the other hand, uses a smaller value of  $g_{\rho NN(1535)} = 4.5$  and leaves the other parameters unchanged. In model 3, in addition to the  $\rho$  exchange, the pseudoscalar meson exchanges  $\pi^0$  and  $\eta$  are also taken into account. This model uses PS-type couplings (as in model 1) for both  $g_{\pi NN^*}$  and  $g_{\eta NN^*}$  for all  $N^*$  resonances, but with the lower values for  $g_{\pi NN(1710)}$  and  $g_{\eta NN(1710)}$ ; see Table II of Appendix A. Again, the same values were used for the  $\rho NN^*$  couplings as in the model 1. The important difference here is the change of  $\Lambda_{\text{sup}}$  parameter that occurs in (2.11), from 4 to 2 GeV. It should be stressed again that, for all the models considered, the calculations for the nucleon resonances  $N(1535)$ ,  $N(1650)$ ,  $N(1710)$ , and  $N(1880)$  were performed using the coupling constants  $g_{\pi NN^*}$  and  $g_{\eta NN^*}$  from Table II of Appendix A and  $g_{\rho NN^*}$  from the analysis in Appendix C.

Figure 3 shows results of integrated cross sections for the exclusive  $\eta$  meson production as a function of center-of-mass (c.m.) energy  $\sqrt{s}$  together with experimental data. Model results include the  $\eta$ -bremsstrahlung mechanism with the intermediate nucleon ( $N$ ), the nucleon resonance contributions, and the  $VV$ -fusion contributions. The coherent sum of all contributions, which of course includes the interference term between them, is denoted by the black solid line (“total, model 1”). The individual contributions included in the amplitude are also shown. One can see that the  $N(1535)$  component dominates. The results calculated for the  $N^*$  contributions excited by the  $\rho$  exchange reproduce energy dependence of the measured  $pp \rightarrow pp\eta$  cross section.

It is worthwhile to review, even briefly, the experimental data for the  $pp \rightarrow pp\eta$  reaction, which can be found in the literature. The experimental data in Fig. 3 displayed as solid circles ( $\bullet$ ) are from the HEP-Data repository [64], [65], and [66–72]. Some experimental results were corrected for the branching ratio  $\mathcal{B}(\eta \rightarrow \pi^+ \pi^- \pi^0) = 23.02\%$  from [73]. Figure 3 presents

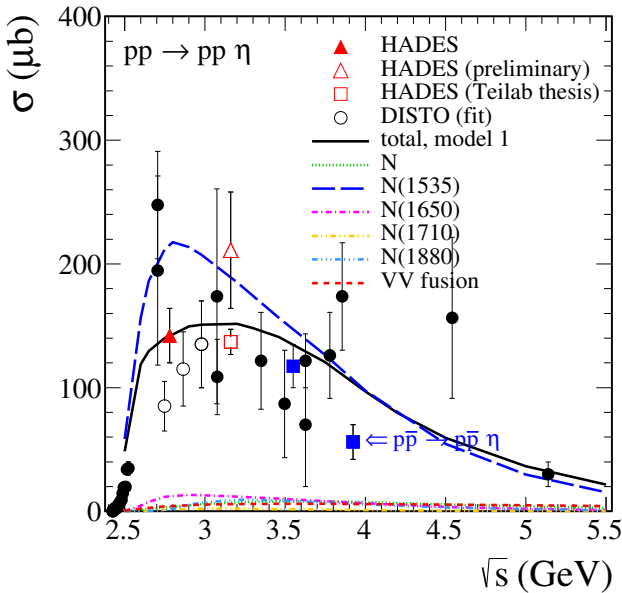


FIG. 3. Total cross section for the  $pp \rightarrow pp\eta$  reaction as a function of collision energy  $\sqrt{s}$ . Shown are the complete model result (“total, model 1”) and the individual contributions included in the calculations together with the compilation of experimental data. The data points from the figure legend are referenced in the text. There are also shown two experimental points corresponding to  $p\bar{p} \rightarrow p\bar{p}\eta$ .

also two experimental points (■) which correspond to the  $p\bar{p}$  interactions [74, 75]. Clearly, the bubble chamber experimental data are not precise enough to provide a quantitative constraint on the theoretical model. The DISTO Collaboration [24] measured the  $pp \rightarrow pp\eta$  reaction in the  $\eta \rightarrow \pi^+\pi^-\pi^0$  decay channel at three c.m. en-

ergies  $\sqrt{s} = 2.748, 2.865$ , and  $2.978$  GeV (at proton beam kinetic energies  $E_{\text{kin}} = 2.15, 2.50$ , and  $2.85$  GeV, respectively). The data points marked as (○) in Fig. 3 are taken from [24] and have been estimated by the DISTO Collaboration; see [76] for a description of the method used. It is important to mention that the DISTO Collaboration does not provide values for the total cross section for the  $pp \rightarrow pp\eta$  reaction, but only an absolute normalization of their data (based on fits of data with  $\sqrt{s}$  ranging from threshold up to  $3.4$  GeV and without taking into account both results of Pickup *et al.* [66] at  $\sqrt{s} = 2.7$  GeV). The data point marked as (▲) was obtained by the HADES Collaboration [27]. In this experiment, the exclusive  $\eta$  production in  $pp$  collisions was studied in hadronic ( $\eta \rightarrow \pi^+\pi^-(\pi^0)$ ) and leptonic ( $\eta \rightarrow \gamma e^+e^-$ ) channels at  $E_{\text{kin}} = 2.2$  GeV ( $\sqrt{s} = 2.78$  GeV). The extracted cross section of  $\sigma = 142 \pm 22 \mu\text{b}$  by HADES Collaboration has a larger value than those obtained by DISTO Collaboration in a similar energy range. In Ref. [25] the preliminary total production cross section  $\sigma = 211 \pm 47 \mu\text{b}$  for  $\sqrt{s} = 3.16$  GeV ( $E_{\text{kin}} = 3.5$  GeV) was determined. The result  $\sigma = 136.9 \pm 0.9 \text{ (stat)} \pm 10.1 \text{ (syst)} \mu\text{b}$  from Teilab’s thesis [26] seems to be inconsistent with the result of [25]. Note the very small error in the estimation from [26]. The HADES experiment at  $\sqrt{s} = 3.46$  GeV ( $E_{\text{kin}} = 4.5$  GeV) will provide further important information on the exclusive  $\eta$  production; see [28, 29] for some details on the analysis.

The integrated cross sections for the  $pp \rightarrow pp\eta$  reaction from  $\sqrt{s} = 2.748$  to  $8.0$  GeV for three models are given in Table I. For model 1 the cross sections of the individual contributions are also shown. The complete results for models 2 and 3 are summarized at the end of the table. Presented theoretical results for different models can be used as a prediction for future experiments on the  $pp \rightarrow pp\eta$  reaction.

TABLE I. Cross sections (in  $\mu\text{b}$ ) for the  $pp \rightarrow pp\eta$  reaction calculated for  $\sqrt{s}$  from  $2.748$  to  $8.0$  GeV. Results for the individual contributions and their coherent sum (“Total, model 1”) for model 1 are given. The last two columns contain the complete results for models 2 and 3.

$\sqrt{s}$ (GeV)	Total, model 1	$\sigma$ ( $\mu\text{b}$ )								
		$N$	$N(1535)$	$N(1650)$	$N(1710)$	$N(1880)$	VV fusion	Total, model 2	Total, model 3	
2.748		139.0	3.1	212.1	11.6	1.3	0.9	3.9	111.9	174.6
2.978		149.1	5.7	208.1	13.0	2.1	7.1	5.3	129.4	143.9
3.46		136.9	8.0	156.5	10.2	1.7	8.8	6.1	116.2	80.8
5.0		37.1	3.9	34.4	2.3	0.3	1.9	4.8	31.9	21.1
8.0		3.3	0.7	0.3	0.02	< 0.003	0.01	2.5	3.3	5.4

From Fig. 3 and Table I one can see that the  $VV$ -fusion contributions are much lower than the experimental data. The cross section from the  $VV \rightarrow \eta$  fusion quickly rises from the reaction threshold  $\sqrt{s_{\text{thr}}} = 2m_p + m_\eta$ , it reaches a maximum about  $\sqrt{s} \approx 3.46$  GeV, and then it starts to decrease towards higher energies. It should

be mentioned that without the reggeization effect, calculated according to (2.23)–(2.26), the cross section would continuously grow from the threshold. The reduction of cross section due to the reggeization is about a factor of 10 at  $\sqrt{s} = 3.46$  GeV. Both the HADES and PANDA experiments have a good opportunity to verify this sizable

effect of the model. The  $VV$ -fusion contribution has different characteristics than the bremsstrahlung processes, and as can be seen from Table I, it turns out to be more significant at higher energies.

For the  $\eta$ -bremsstrahlung mechanism with the intermediate proton exchange (contribution denoted by  $N$  in Table I) different type of processes were included in the calculations, i.e., the pre- and post-emission diagrams of Fig. 1 with the  $\pi^0$ ,  $\eta$ ,  $\rho^0$ , and  $\omega$  exchanges. For model 1, the total cross section for  $\sqrt{s} = 3.46$  GeV is  $\sigma_{N,\text{total}} = 8.02 \mu\text{b}$ . It is instructive to give the relative contribution to the cross section for each exchange. The results are as follows:  $\sigma_{N,\pi^0} = 1.47 \mu\text{b}$ ,  $\sigma_{N,\eta} = 0.9 \text{ nb}$ ,  $\sigma_{N,\rho^0} = 2.08 \mu\text{b}$ , and  $\sigma_{N,\omega} = 2.43 \mu\text{b}$ . Clearly, the larger total cross-section value indicates interference effect between different exchanges in amplitude. It is noteworthy that the predominant  $N$  contribution to the cross-section comes from pre-emission diagrams (a) and (c) of Fig. 1 than from post-emission diagrams (b) and (d) of Fig. 1. There is also interference between them. For the pre-emission diagrams one finds  $\sigma_{N,\text{pre}} = 8.52 \mu\text{b}$ , while for the post-emission diagrams one finds only  $\sigma_{N,\text{post}} = 0.26 \mu\text{b}$ . One can see from Table I that the  $N$  contribution calculated within model 1 is important even going to higher collision energies. For models 2 and 3, the  $N$  contribution is less significant (see the results of Figs. 4 and 7 below) because there for  $\rho$  and  $\omega$  exchange contributions the more restricting parameter  $\Lambda_{\text{sup}} = 2$  GeV in (2.11) was assumed. These predictions represent my educated guesses for the cross sections, the validity of which is to be determined by comparison to future data.

In Figs. 4-6, results obtained in models 1 and 2 are presented. Figures 4 and 5 show the distributions in  $\cos \theta_\eta$ ,  $p_\eta$  and  $M_{p\eta}$ ,  $M_{pp}$ , respectively. As explained above, several mechanisms for exclusive  $\eta$  meson production were included. Their individual contributions and the coherent sum (details in legend and description of Fig. 4) for the two models 1 and 2 are presented. One can see that the contribution of  $N(1535)$  (through  $\rho$  exchange) is dominant and that there is a large interference of different components in the amplitude. The shape of complete theoretical predictions of  $\cos \theta_\eta$  and  $p_\eta$  seems to be in good agreement with the DISTO data [24]. The experimental data points were normalized to the values of the total cross sections from [24] and include both statistical and the relative systematical uncertainties, but do not include additional global systematic uncertainties of the absolute scale of 22% and 33% for  $\sqrt{s} = 2.748$  and 3.46 GeV, respectively.

Figure 6 shows the distribution in Feynman- $x$  variable for the  $\eta$  meson (defined as  $x_{F,\eta} = 2p_{z,\eta}/\sqrt{s}$  with the longitudinal momentum of the meson in the c.m. system) and the distributions in meson transverse momentum  $p_{t,\eta}$  and proton transverse momentum  $p_{t,p}$  for  $\sqrt{s} = 3.46$  GeV. From these and previous results, one can see that it is difficult to separate the  $VV$ -fusion con-

tribution (indicated by the red short-dashed line) from others. However, this contribution plays an increasingly important role at higher energies. On the other hand, the contribution of the non-resonant bremsstrahlung (indicated by the green dotted line) is significant in the region of  $\cos \theta_\eta \approx \pm 1$ ,  $p_\eta \approx 1$  GeV, and for  $|x_{F,\eta}| \approx 0.55$ . The nucleonic contribution is also characterized by smaller values of the  $pp$  invariant mass and the  $\eta$  and  $p$  transverse momenta. Experimental observation of an enhancement in these kinematic regions can be used to determine the magnitude of the nucleonic term, at least the strength of the  $\eta NN$  coupling.

Figures 7 and 8 represent the differential cross sections for model 3. It can be seen from Fig. 7 that with increasing energy, the contribution of  $N^*$  resonances excited via  $\pi^0$  exchange becomes more significant than the  $N^*$  term excited via  $\rho^0$  exchange. The predictions of model 3 with the admixture of pseudoscalar meson exchanges describe the DISTO angular distributions less accurately than models 1 and 2 (see Fig. 4) as far as the shape of the distributions is concerned. The importance of the  $N(1710)$  and  $N(1880)$  resonances is more visible in model 3 [see two distinct resonant bumps after  $N(1535)$  in  $d\sigma/dM_{p\eta}$ ]. Such prediction of the model (resonant features) may be verified by examining the distributions in the proton transverse momentum and in the  $\eta p$  invariant mass. In particular, compared to  $\rho$  exchange processes, excited states by pseudoscalar meson exchanges have the  $d\sigma/dp_{t,p}$  distribution shifted towards smaller values.

Figure 9 shows the two-dimensional differential cross sections in the  $M_{p\eta}^{(1)}-M_{p\eta}^{(2)}$  plane (left panels) and in the  $M_{p\eta}^{(1)}-M_{pp}$  plane (right panels) calculated for model 1 (top panels) and for model 3 (bottom panels). The resonance structure is clearly visible in both models with dominance of  $N(1535)$ . Model 3 highlights the possible role of heavier states  $N(1710)$  and  $N(1880)$  due to the inclusion of pseudoscalar meson excitations. These resonance patterns provide crucial information about the reaction mechanism and can be used as benchmarks for experimental analysis.

At higher energies other fusion mechanisms may be important. As discussed in [34, 35], the Pomeron-Pomeron-fusion mechanism and the subleading Reggeon exchanges (Pomeron- $f_{2R}$ ,  $f_{2R}$ -Pomeron,  $f_{2R}$ - $f_{2R}$ ) seem to dominate at WA102 energy of  $\sqrt{s} = 29.1$  GeV. The inclusion of secondary Reggeons in the calculation seems to be particularly important to explain the available data from experiments at intermediate energies. It can be expected that these processes will give a rather small contribution up to  $\sqrt{s} \approx 5$  GeV. To quantify the diffractive mechanism in the intermediate energy range and to understand the role of subleading exchanges, future measurements of exclusive meson production from the FAIR accelerator (SIS100) would be necessary.

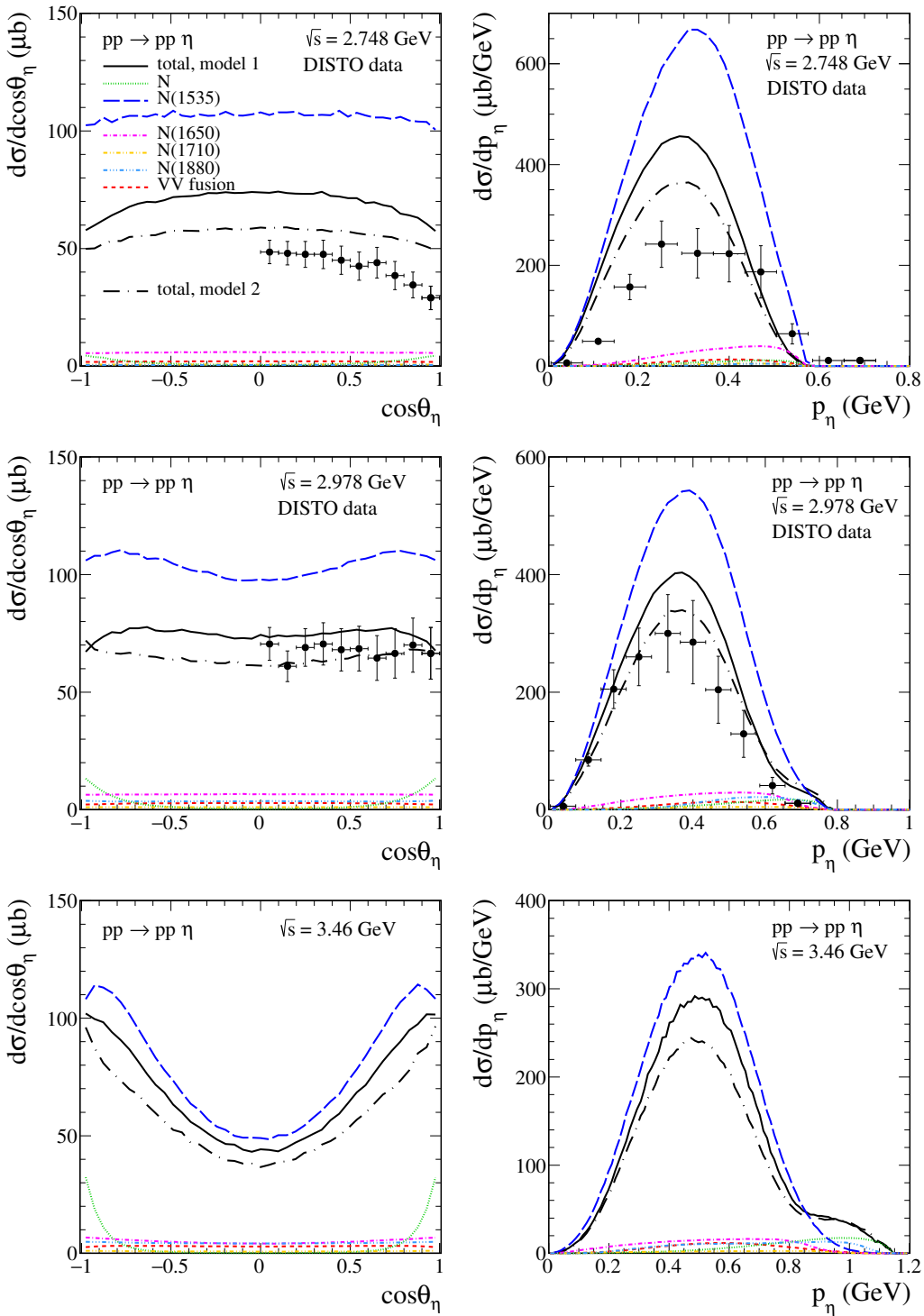


FIG. 4. Differential cross sections  $d\sigma/d\cos\theta_\eta$  and  $d\sigma/dp_\eta$  for the  $pp \rightarrow pp\eta$  reaction at  $\sqrt{s} = 2.748, 2.978, 3.46$  GeV. The experimental data points are from [24]. The black solid line presents the coherent sum for the model 1, while the black long-dashed-dotted line corresponds to calculation for the model 2. The individual contributions for the model 1 are also shown.

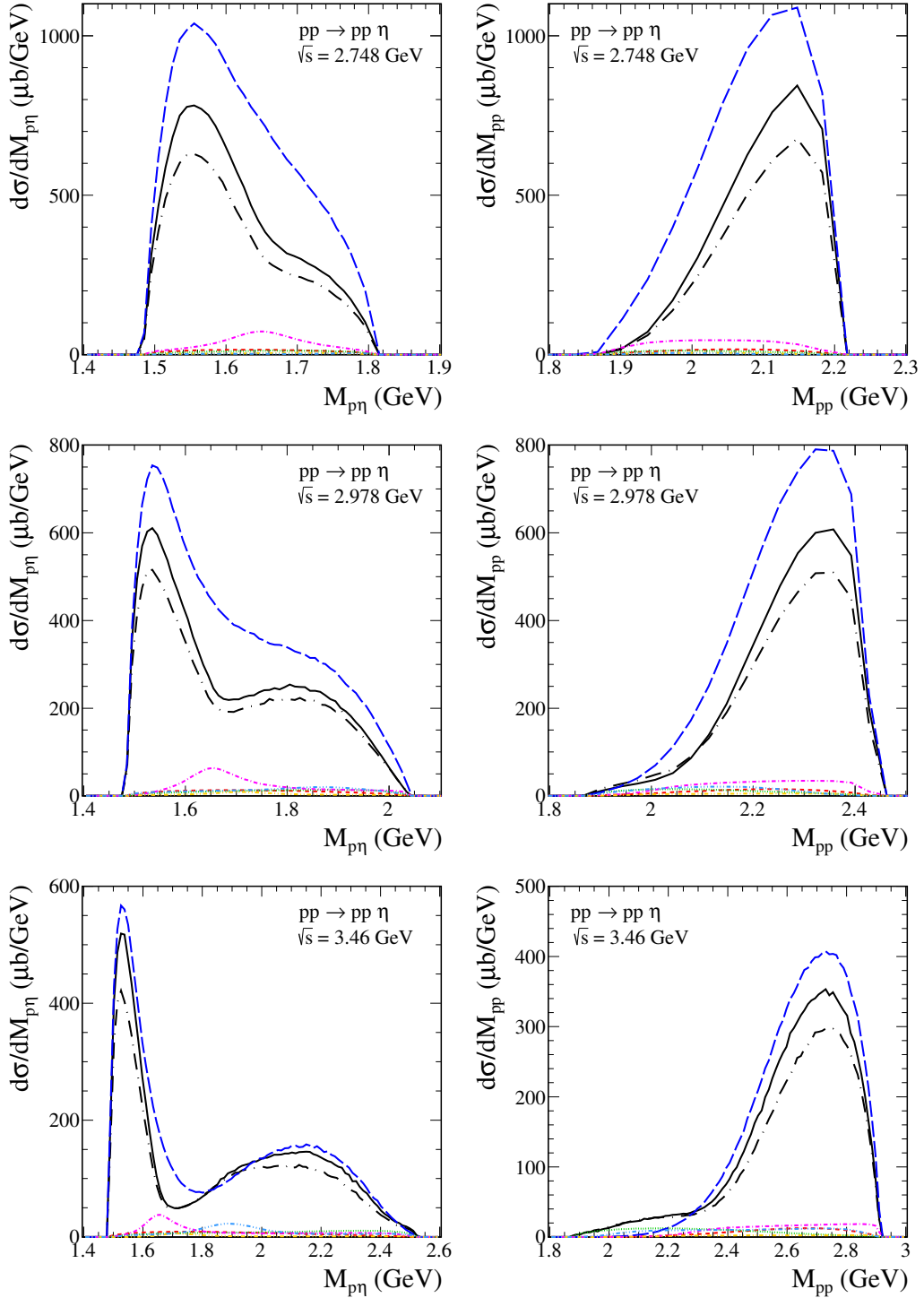


FIG. 5. Differential cross sections  $d\sigma/dM_{p\eta}$  and  $d\sigma/dM_{pp}$  for the  $pp \rightarrow pp\eta$  reaction at  $\sqrt{s} = 2.748, 2.978, 3.46$  GeV. The meaning of the lines is the same as in Fig. 4.

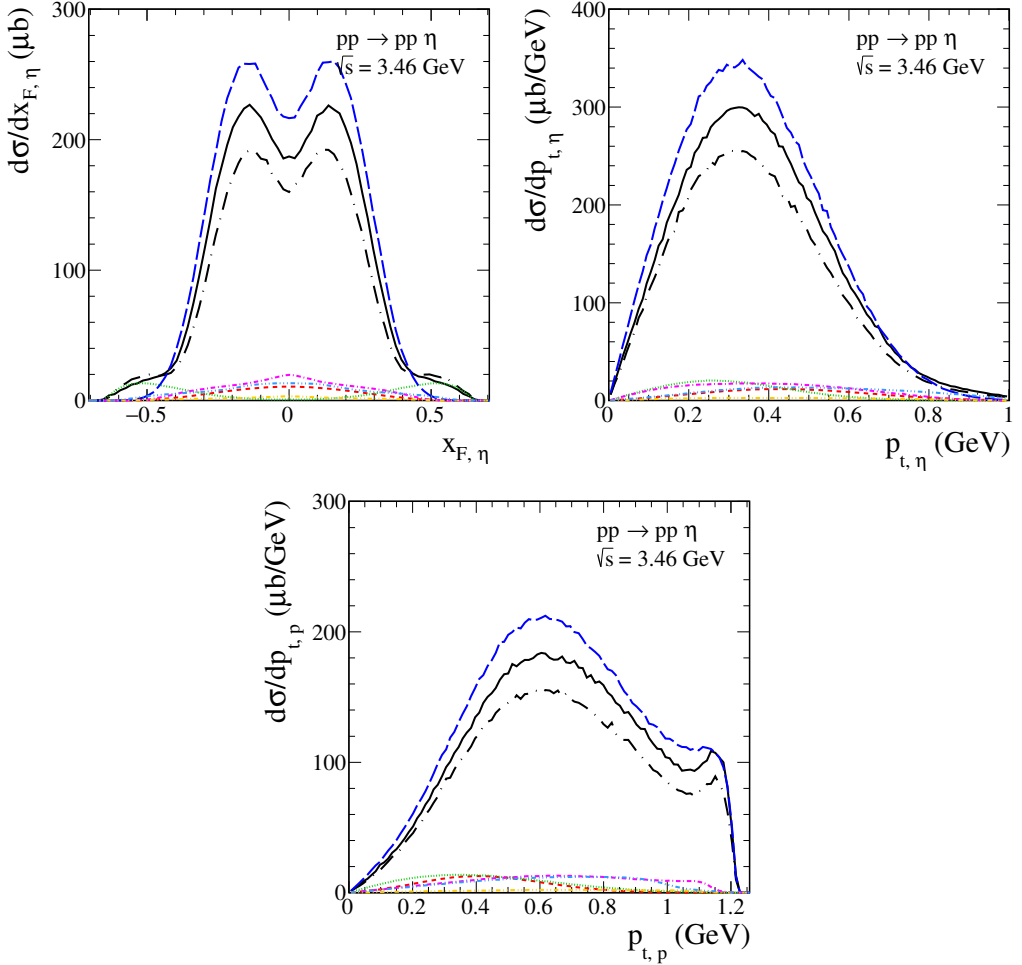


FIG. 6. Differential cross sections for the  $pp \rightarrow pp\eta$  reaction at  $\sqrt{s} = 3.46 \text{ GeV}$ . The meaning of the lines is the same as in Fig. 4.

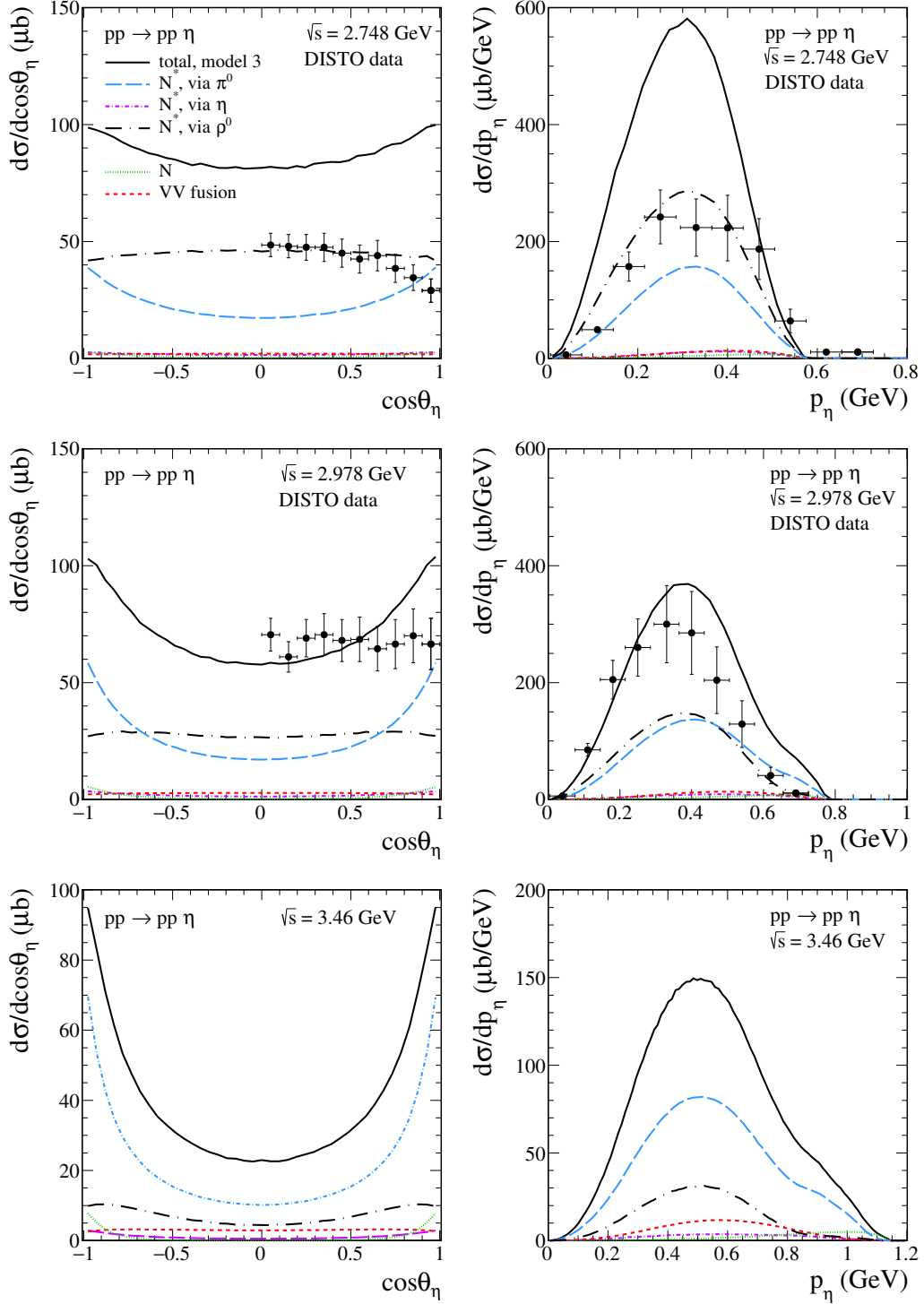


FIG. 7. Differential cross sections  $d\sigma/d\cos\theta_\eta$  and  $d\sigma/dp_\eta$  for the  $pp \rightarrow pp\eta$  reaction at  $\sqrt{s} = 2.748, 2.978, 3.46$  GeV. The experimental data points are from [24]. The results for model 3 are shown. The black solid line represents the coherent sum of all contributions ( $N$ ,  $VV$  fusion, and  $N^*$  terms). The blue long-dashed line represents the result for  $N^*$  resonances excited via  $\pi^0$  exchange, the violet short-dashed-dotted corresponds to  $N^*$  contribution via  $\eta$  exchange, and the black long-dashed-dotted line corresponds to  $N^*$  contribution via  $\rho^0$  exchange.

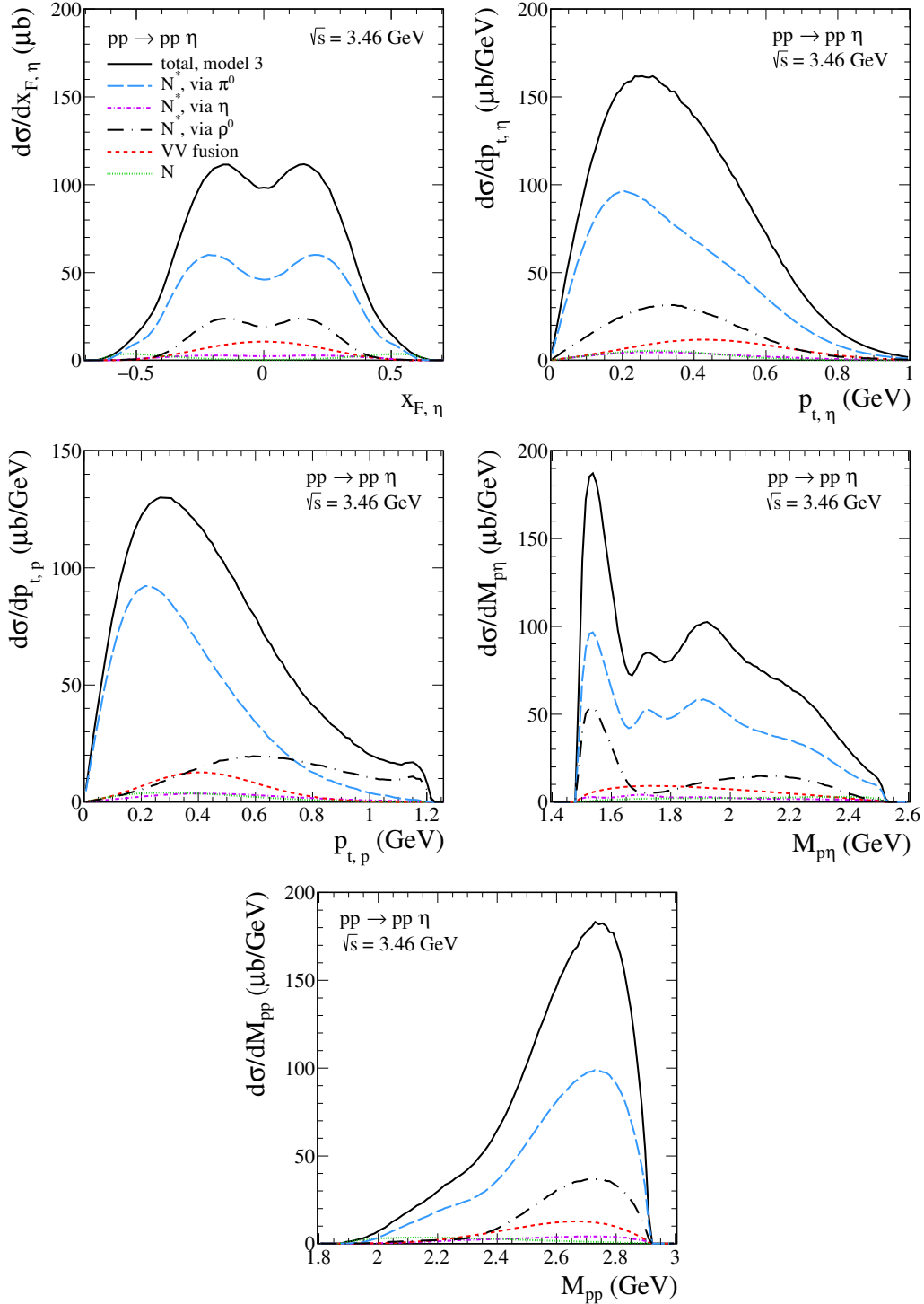


FIG. 8. Differential cross sections for the  $pp \rightarrow pp\eta$  reaction at  $\sqrt{s} = 3.46$  GeV. The meaning of the lines is the same as in Fig. 7.

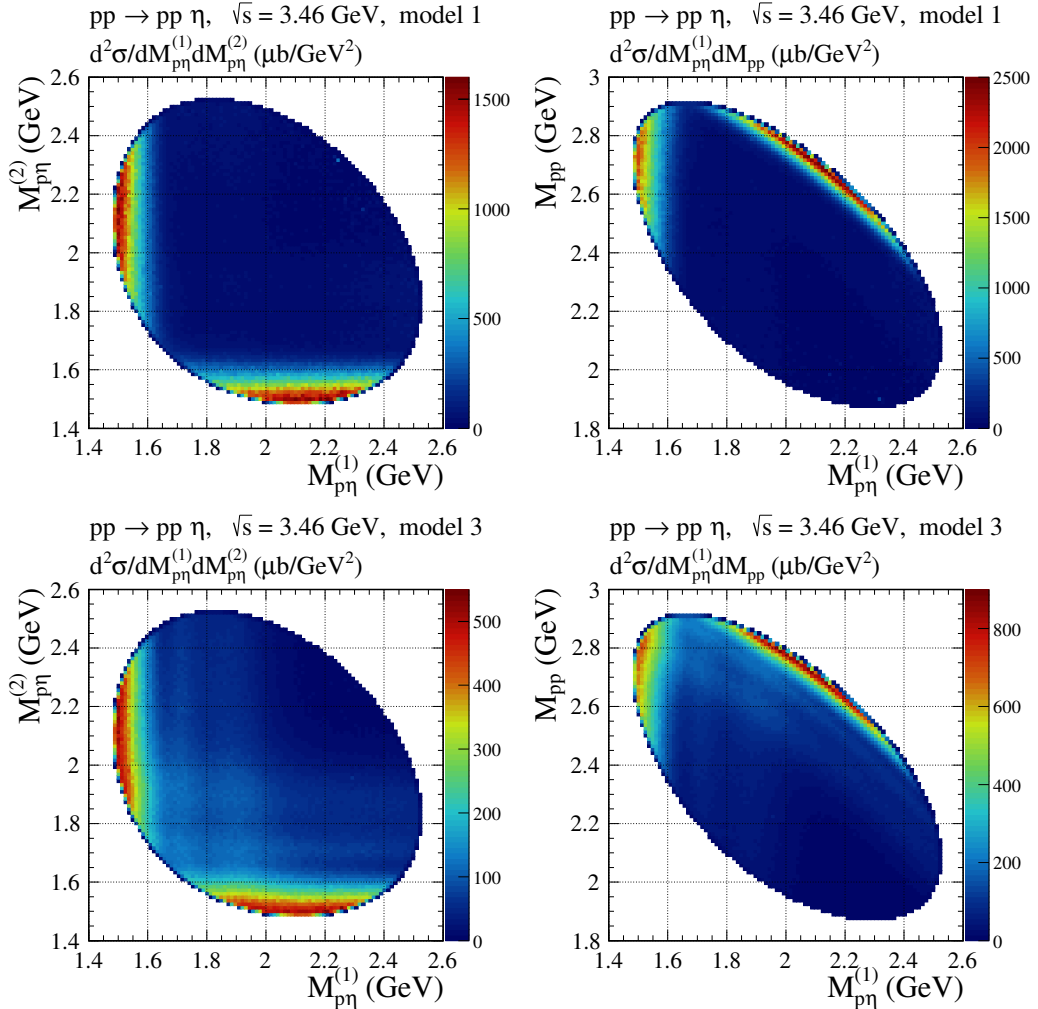


FIG. 9. The two-dimensional distributions in  $(M_{p\eta}^{(1)}, M_{p\eta}^{(2)})$  and in  $(M_{p\eta}^{(1)}, M_{pp})$  for the  $pp \rightarrow pp\eta$  reaction for model 1 (top panels) and for model 3 (bottom panels) calculated for  $\sqrt{s} = 3.46$  GeV.

#### IV. SUMMARY AND CONCLUSIONS

The present study investigates the  $\eta$  meson exclusive production in the  $pp \rightarrow pp\eta$  reaction at energies relevant for the HADES, PANDA, and SIS100 experiments at GSI-FAIR. The production mechanism was studied by using an effective Lagrangian approach. Concretely, the  $\eta$ -bremsstrahlung mechanism with the intermediate proton exchange via the  $\pi^0$ ,  $\eta$ ,  $\rho^0$ , and  $\omega$  exchanges, the mechanism with an excitation of nucleon resonances [ $N(1535)$ ,  $N(1650)$ ,  $N(1710)$ ,  $N(1880)$ ] via the pseudoscalar- or/and vector-meson exchanges (depends on the model), as well as the  $\omega\omega$ - and  $\rho^0\rho^0$ -fusion mechanism were considered. The model results have been compared with the available DISTO [24] and HADES [25–27] data. The numerical analysis indicates that the  $N(1535)$  contribution is the most important process at lower energies, but other contributions cannot be omitted due to interference effects. Resonances like  $N(1650)$ ,  $N(1710)$ ,  $N(1880)$  and vector-meson fusion processes contribute significantly to the considered reaction, but their relative importance has to be verified by experiment.

To determine the parameters of the model, the  $\pi^- p \rightarrow \eta n$  and  $\gamma p \rightarrow \eta p$  reactions were discussed. An attempt was made to describe both integrated and differential cross-section data for these processes, in which the nucleon resonances play a crucial role. The use of reggeized- $\rho$  and - $\omega$  exchanges for the photoproduction of the  $\eta$  meson is justified at higher energies and in the forward scattering region. There are new CLAS experimental data [48]. By comparing the model to experimental data for  $\pi^- p \rightarrow \eta n$  and  $\gamma p \rightarrow \eta p$ , the form factors and the cutoff parameters occurring in the vertices were fixed. The coupling constants  $g_{VV\eta}$  ( $V$  stands for  $\rho^0$  or  $\omega$ ) were extracted from the radiative decay rates of  $V \rightarrow \eta\gamma$  using an effective Lagrangian approach and a vector-meson-dominance ansatz. The  $\pi NN^*$  and  $\eta NN^*$  coupling constants are known from the relevant partial decay widths; see Table II in Appendix A. The  $\rho NN^*$  coupling constants can be constrained by the available experimental data from the radiative decays  $N^* \rightarrow N\rho^0 \rightarrow N\gamma$  as shown in Appendix C. Additionally, the  $N(1535) \rightarrow N\rho^0 \rightarrow N\pi^+\pi^-$  decay was discussed. These findings showed that the  $\rho NN^*$  coupling constants are very sensitive to the off-shell effects of the intermediate  $\rho^0$  meson.

The results presented in this work provide valuable theoretical guidance for future experimental efforts aimed at measuring the  $pp \rightarrow pp\eta$  reaction at intermediate energies. The way in which the nucleon resonances are excited is the reason for the discrepancy between the theoretical results (models 1–3) and the DISTO experimental data measured at proton-proton collision energies  $\sqrt{s} = 2.748 - 2.978$  GeV. This is mainly a matter of the  $N(1535)$  resonance created by the exchange of virtual pseudoscalar and/or vector mesons. The angular

distribution of the  $\eta$  meson ( $d\sigma/d\cos\theta_\eta$ ) should be forward peaked if  $\pi^0$  plus  $\eta$  exchanges (or  $\sigma$  exchange not included in the present calculations) are dominant processes in the bremsstrahlung mechanism. When compared to the DISTO differential cross-section data, one finds that a model with the dominance of the  $\rho$  exchange is the preferred option. The  $VV$ -fusion mechanism plays an important role at higher energies. To learn more about the relevant reaction mechanism, a detailed analysis of observables other than the total cross section, such as the invariant mass distributions of the  $\eta p$  and  $pp$  systems, the polar angle and momentum distributions of the  $\eta$  meson, and the transverse momentum distribution of the proton, seems necessary.

Total and differential cross sections for the  $pp \rightarrow pp\eta$  reaction for the HADES experiment at  $\sqrt{s} = 3.46$  GeV are provided. The calculations were also done at  $\sqrt{s} = 5.0$  GeV (PANDA) and  $\sqrt{s} = 8.0$  GeV (SIS100). The results can serve as a prediction for the already performed HADES [28, 29] and may offer a new perspective for planned PANDA and SIS100 [31] measurements at GSI. Upcoming experiments in the intermediate energy range will be crucial for validating theoretical predictions presented here, and will be especially useful if they provide accurate data accounting for differential distributions in several variables. This is important for clarifying the production mechanism in the considered kinematic range and checking different models for the FSI and ISI effects (not included in the current analysis). Further measurements would be useful to confirm the theoretical findings, particularly those concerning the role of excited  $N^*$  resonances and  $VV$ -fusion processes, as well as the interplay between them. Related works on the  $pp \rightarrow pp\eta'$ ,  $pp \rightarrow pp\omega$ , and  $pp \rightarrow pp\phi$  reactions are currently in progress and will appear elsewhere.

#### ACKNOWLEDGMENTS

I would like to thank I. Ciepał, P. Salabura, A. Szczurek, and M. Zieliński for useful comments.

#### Appendix A: The reaction $\pi^- p \rightarrow \eta n$ , effective coupling Lagrangians, propagators, and form factors

In this section, the  $\pi^- p \rightarrow \eta n$  reaction shown in Fig. 10 is discussed. The differential cross section is given by

$$\frac{d\sigma}{d\Omega} = \frac{1}{64\pi^2 s} \frac{|k_\eta|}{|k_\pi|} \frac{1}{2} \sum_{\text{spins}} |\mathcal{M}_{\pi^- p \rightarrow \eta n}|^2, \quad (\text{A1})$$

where  $k_\pi$  and  $k_\eta$  are the c.m. three-momenta of the initial  $\pi^-$  and the final  $\eta$  mesons, respectively. The amplitude can be expressed as a sum of the  $s$ -,  $t$ -, and  $u$ -channel pole diagrams:  $\mathcal{M}_{\pi^- p \rightarrow \eta n} = \mathcal{M}_s + \mathcal{M}_t + \mathcal{M}_u$ . In the present work, the  $n$  and neutral  $N^*$  exchanges in

the  $s$  channel and the  $p$  exchange in the  $u$  channel are taken into account. For simplicity, the charged  $N^*$  exchanges in the  $u$  channel and the  $a_0$ -meson exchange in

the  $t$ -channel are neglected. The  $N^*$ -resonance contributions in the  $u$ -channel are suppressed by the kinematics [see the discussion after Eqs. (A20), (A21)].

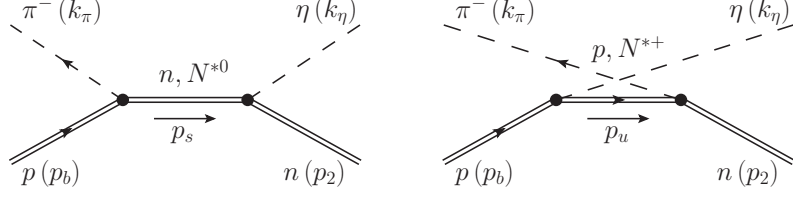


FIG. 10. Diagrams for the  $\pi^- p \rightarrow \eta n$  reaction with baryon exchanges in the  $s$ - and  $u$ -channel.

The amplitude  $\mathcal{M}_{\pi^- p \rightarrow \eta n}$  reads

$$\begin{aligned} \mathcal{M}_{\pi^- p \rightarrow \eta n} &= \mathcal{M}_s^{(n)} + \mathcal{M}_u^{(p)} + \sum_{N_{1/2}^*} \mathcal{M}_s^{(N_{1/2}^*)} + \sum_{N_{3/2}^*} \mathcal{M}_s^{(N_{3/2}^*)} \\ &= \bar{u}_n(p_2, \lambda_2) \{ \Gamma^{(\eta nn)}(k_\eta) S^{(n)}(s) \Gamma^{(\pi^- pn)}(k_\pi) + \Gamma^{(\pi^- np)}(k_\pi) S_F^{(p)}(u) \Gamma^{(\eta pp)}(k_\eta) \\ &\quad + \sum_{N_{1/2}^*} \Gamma^{(\eta n N_{1/2}^*)}(k_\eta) P^{(N_{1/2}^*)}(s) \Gamma^{(\pi^- p N_{1/2}^*)}(k_\pi) \\ &\quad + \sum_{N_{3/2}^*} \Gamma^{\mu(\eta n N_{3/2}^*)}(k_\eta) P_{\mu\nu}^{(N_{3/2}^*)}(s) \Gamma^{\nu(\pi^- p N_{3/2}^*)}(k_\pi) \} u_p(p_b, \lambda_b), \end{aligned} \quad (\text{A2})$$

where  $s = W_{\pi^- p}^2 = p_s^2$  and  $p_s = p_b + k_\pi$ . For the  $u$  channel, the  $\pi NN$  and  $\eta NN$  vertices need to be interchanged and there is an exchange of charge particles in the middle of the diagram, with  $u = p_u^2$ ,  $p_u = p_b - k_\eta$ . The  $MNN$ ,  $MNN_{1/2}^*$ , and  $MNN_{3/2}^*$  interaction vertices could be read as below with the coupling constants from Table II taking into account isospin factor,  $g_{\pi^- pn} = \sqrt{2}g_{\pi NN}$  and  $g_{\pi^- p N^*} = g_{\pi^- n N^*} = \sqrt{2}g_{\pi NN^*}$ .

The pseudoscalar-meson-nucleon coupling Lagrangians can be written as

$$\mathcal{L}_{\pi NN} = -\frac{g_{\pi NN}}{2m_N} \bar{N} \gamma_5 \gamma_\mu \partial^\mu (\boldsymbol{\tau} \Phi_\pi) N, \quad (\text{A3})$$

$$\begin{aligned} \mathcal{L}_{\eta NN} &= -g_{\eta NN} \\ &\times \bar{N} \left( i\gamma_5 \lambda + (1-\lambda) \frac{1}{2m_N} \gamma_5 \gamma_\mu \partial^\mu \right) \Phi_\eta N, \end{aligned} \quad (\text{A4})$$

where  $N$  and  $\Phi$  denote the nucleon and meson fields, respectively. The parameter  $\lambda$  in (A4) controls the admixture of the two types of couplings: pseudoscalar (PS) ( $\lambda = 1$ ) and pseudovector (PV) ( $\lambda = 0$ ). Note that the  $\pi NN$  coupling constant  $g_{\pi NN}^2/4\pi = 13.4 - 14.4$  [77–79] is much better determined than the  $\eta NN$  coupling constant. The  $\pi NN$  coupling is preferred to be pseudovector [80]; however, there is no compelling reason to select the PV coupling rather than the PS form for

the  $\eta NN$  vertex [81, 82]. From fits to  $\eta$  photoproduction of [81] one can deduce that the PS coupling with  $g_{\eta NN}^2/4\pi = 0.4$  is preferred. In [82] the PV admixture was found. More accurate data are needed for further study of the problem. Different values of  $\eta NN$  coupling have been determined/used in the literature, see e.g. [11, 20, 50, 83]. From [77, 78] one has  $g_{\eta NN}^2/4\pi = 0.6 - 6.4$  and even smaller  $g_{\eta NN}^2/4\pi \lesssim 0.1$  [20, 53]. The coupling for the  $\eta NN$  vertex is uncertain, but significantly smaller than the  $\pi NN$  coupling. In this work,  $g_{\pi NN}^2/4\pi = 14.0$  in (A3) is taken. For the  $\eta NN$  coupling (A4) the parameters are taken from [82]:  $\lambda = 0.504$  and  $g_{\eta NN} \rightarrow g_\eta = g_{\eta NN}/\lambda = f_{\eta NN}/(1-\lambda) = 4.03$ .

The  $\Gamma^{(MNN_{1/2}^*)}$  vertices involving spin-1/2 nucleon resonances obtained from the effective Lagrangians are [11, 20, 60, 77]

$$\mathcal{L}_{\pi NN_{1/2}^*}^{\text{PS}} = \pm i g_{\pi NN^*} \bar{N}^* \left( \frac{1}{\gamma_5} \right) (\boldsymbol{\tau} \Phi_\pi) N + \text{h.c.}, \quad (\text{A5})$$

$$\mathcal{L}_{\eta NN_{1/2}^*}^{\text{PS}} = \pm i g_{\eta NN^*} \bar{N}^* \left( \frac{1}{\gamma_5} \right) \Phi_\eta N + \text{h.c.}, \quad (\text{A6})$$

$$\begin{aligned} \mathcal{L}_{\pi NN_{1/2}^*}^{\text{PV}} &= \pm \frac{g_{\pi NN^*}}{m_{N^*} \mp m_N} \bar{N}^* \left( \frac{\gamma_\mu}{\gamma_5 \gamma_\mu} \right) \partial^\mu (\boldsymbol{\tau} \Phi_\pi) N \\ &\quad + \text{h.c.}, \end{aligned} \quad (\text{A7})$$

$$\mathcal{L}_{\eta NN_{1/2^\mp}^*}^{\text{PV}} = \pm \frac{g_{\eta NN^*}}{m_{N^*} \mp m_N} \bar{N}^* \begin{pmatrix} \gamma_\mu \\ \gamma_5 \gamma_\mu \end{pmatrix} \partial^\mu \Phi_\eta N + \text{h.c.}, \quad (\text{A8})$$

where the upper (lower) sign and factor in parentheses correspond to negative-parity (positive-parity) resonances. For the  $\pi NN^*$  and  $\eta NN^*$  vertices one has the choice of (pseudo-)scalar (PS) or (pseudo-)vector (PV) couplings; i.e., scalar and vector in the case of an odd parity resonance, and pseudoscalar and pseudovector in the case of an even parity resonance. The PS and PV couplings are equivalent when both baryons are on their mass shell.

Note that in [84] the PS coupling is used in the case of odd-parity  $S_{11}$  resonances (with the incoming partial wave notation  $L_{2I,2S}$ ), and the PV form in the case of even-parity  $P_{11}$  resonances (just as in the nucleon case). As was mentioned there, this choice of PS-PV coupling for the resonances is supported by the fact, that in the  $\pi N \rightarrow \pi N$  partial wave data, the resonant structures are more pronounced in the  $S$  wave ( $J^P = 1/2^-$ ) than in the  $P$  wave ( $J^P = 1/2^+$ ). In [19] the calculations for the  $pp \rightarrow pp\eta$  reaction were done with two types of couplings, PS and PV, and little difference was found there; see Fig. 10 of [19]. In principle one can select a linear combination of both and fit the PS/PV ratio to the data [20].

The  $\Gamma_\mu^{(MNN_{3/2}^*)}$  vertices involving spin-3/2 nucleon resonances can be written as [11, 18, 77]

$$\mathcal{L}_{\pi NN_{3/2^\mp}^*} = \frac{g_{\pi NN^*}}{m_\pi} \bar{N}^{*\mu} \Theta_{\mu\nu}(z) \begin{pmatrix} \gamma_5 \\ 1 \end{pmatrix} \partial^\nu (\tau \Phi_\pi) N + \text{h.c.}, \quad (\text{A9})$$

$$\mathcal{L}_{\eta NN_{3/2^\mp}^*} = \frac{g_{\eta NN^*}}{m_\eta} \bar{N}^{*\mu} \Theta_{\mu\nu}(z) \begin{pmatrix} \gamma_5 \\ 1 \end{pmatrix} \partial^\nu \Phi_\eta N + \text{h.c.}, \quad (\text{A10})$$

where  $\Theta_{\mu\nu}(z) = g_{\mu\nu} - (A(1+4z)/2 + z)\gamma_\mu\gamma_\nu$ . The choice of the so-called “off-shell parameter”  $z$  is arbitrary and it is treated as a free parameter to be determined by fitting to the data; see Table XII of [85] and Table V of [84]. Following Refs. [11, 18], for simplicity, the values  $A = -1$  and  $z = -1/2$  are adopted.

The partial decay widths of the nucleon resonances are calculated from the above Lagrangian couplings as follows:

$$\Gamma(N_{1/2^\mp}^* \rightarrow NM) = f_{\text{ISO}} \frac{g_{MNN^*}^2}{4\pi} p_N \frac{E_N \pm m_N}{m_{N^*}}, \quad (\text{A11})$$

$$\Gamma(N_{3/2^\mp}^* \rightarrow NM) = f_{\text{ISO}} \frac{g_{MNN^*}^2}{12\pi} \frac{p_N^3}{m_M^2} \frac{E_N \mp m_N}{m_{N^*}}, \quad (\text{A12})$$

where the upper (lower) sign corresponds to negative-parity (positive-parity) resonance. Above,  $p_N = |\mathbf{p}_N| =$

$\lambda(m_{N^*}^2, m_N^2, m_M^2)/(2m_{N^*})$  and  $E_N = \sqrt{p_N^2 + m_N^2}$  denote the absolute value of the three-momentum and energy of the nucleon in the rest frame of  $N^*$ , respectively. Here,  $\lambda$  denotes the Källén function with  $\lambda(x, y, z) \equiv \sqrt{(x-y-z)^2 - 4yz}$ . Furthermore, the isospin factor  $f_{\text{ISO}}$  is equal to 3 for decays into mesons with isospin one ( $\pi$ ), and to 1 otherwise ( $\eta$ ). The absolute value of coupling constants  $g_{MNN^*}$  ( $M = \pi, \eta$ ), could be determined by the experimental decay widths of  $\Gamma(N^* \rightarrow NM)$  in the compilation of the PDG [73]; see Table II.

The propagators  $S_F$  and  $P^{(N_{1/2}^*)}$  of the spin-1/2 for nucleon and resonances, respectively, and  $P_{\mu\nu}^{(N_{3/2}^*)}$  of the spin-3/2 resonances are expressed as

$$iS_F(p^2) = i \frac{\not{p} \pm m_N}{p^2 - m_N^2}, \quad (\text{A13})$$

$$iP^{(N_{1/2}^*)}(p^2) = i \frac{\not{p} \pm m_{N^*}}{p^2 - m_{N^*}^2 + im_{N^*}\Gamma_{N^*}(p^2)}, \quad (\text{A14})$$

$$iP_{\mu\nu}^{(N_{3/2}^*)}(p^2) = i \frac{\not{p} \pm m_{N^*}}{p^2 - m_{N^*}^2 + im_{N^*}\Gamma_{N^*}(p^2)} \mathcal{P}_{\mu\nu}(p), \quad (\text{A15})$$

$$\begin{aligned} \mathcal{P}_{\mu\nu}(p) = & -g_{\mu\nu} + \frac{1}{3} \gamma_\mu \gamma_\nu \pm \frac{1}{3m_{N^*}} (\gamma_\mu p_\nu - \gamma_\nu p_\mu) \\ & + \frac{2}{3m_{N^*}^2} p_\mu p_\nu, \end{aligned} \quad (\text{A16})$$

where  $\pm$  are for the particles and antiparticles, respectively.  $m_{N^*}$  and  $\Gamma_{N^*}$  denote the mass and total width of the  $N^*$  resonance, respectively. The complex term is introduced to take care of the finite width  $\Gamma_{N^*}$  of the unstable nucleon resonance. For a resonance with mass near the  $\eta$  production threshold the approximation of a constant width is not very good and the energy-dependent width is needed; see, e.g., [53, 86–88]. Using a formalism analogous to that in Refs. [53, 88], one can restrict to the dominant decay channels of  $N^* \rightarrow \pi N, \eta N$ , and  $\pi\pi N$ :

$$\Gamma_{N^*}(s) = \Gamma_{\pi N}(s) + \Gamma_{\eta N}(s) + \Gamma_{\pi\pi N}(s), \quad (\text{A17})$$

$$\begin{aligned} \Gamma_{\pi N}(s) = & \mathcal{B}(N^* \rightarrow \pi N) \Gamma_{N^*} \left( \frac{k_\pi(s)}{k_{\pi, N^*}} \right)^{2\ell+1} \\ & \times \left( \frac{X^2 + k_{\pi, N^*}^2}{X^2 + k_\pi^2(s)} \right)^\ell, \end{aligned} \quad (\text{A18})$$

$$\begin{aligned} \Gamma_{\pi\pi N}(s) = & \mathcal{B}(N^* \rightarrow \pi\pi N) \Gamma_{N^*} \left( \frac{k_{2\pi}(s)}{k_{2\pi, N^*}} \right)^{2\ell+4} \\ & \times \left( \frac{X^2 + k_{2\pi, N^*}^2}{X^2 + k_{2\pi}^2(s)} \right)^{\ell+2}. \end{aligned} \quad (\text{A19})$$

The width  $\Gamma_{\eta N}$  has a similar dependence as  $\Gamma_{\pi N}$ . Above  $\ell$  is the orbital angular momentum of a resonance:  $\ell = 0$  for  $N(1535), N(1650), N(1895)$ ;  $\ell = 1$  for  $N(1710), N(1720), N(1880), N(2100)$ ;  $\ell = 2$  for  $N(1520), N(1700), N(1900)$ .  $X$  is a damping parameter, which has

been fixed in the present work to  $X = 0.2$  GeV for all resonances.  $\mathcal{B}(N^* \rightarrow \pi N)$  and  $\Gamma_{N^*}$  are the  $\pi N$  branching ratio and total width, respectively. The c.m. momenta of pion and  $\eta$  are denoted by  $k_\pi(s)$  and  $k_\eta(s)$ , respectively.

Here,  $k_\pi(s) = \sqrt{[s - (m_N + m_\pi)^2][s - (m_N - m_\pi)^2]/4s}$  and  $k_{\pi, N^*} \equiv k_\pi(m_{N^*}^2)$ . In (A19),  $k_{2\pi}$  is the momentum of the compound  $(2\pi)$  system with mass  $2m_\pi$ ,  $k_{2\pi, N^*}$  is equal to  $k_{2\pi}$  at  $s = m_{N^*}^2$ , and  $\mathcal{B}(N^* \rightarrow \pi\pi N) = 1 - \mathcal{B}(N^* \rightarrow \pi N) - \mathcal{B}(N^* \rightarrow \eta N)$ . For the  $N(1895)$ ,  $N(1900)$ , and  $N(2100)$  resonances, the relevant  $\eta' N$  width is also taken into account. The expression is similar to (A18) but with  $\mathcal{B}(N^* \rightarrow \pi N) \rightarrow \mathcal{B}(N^* \rightarrow \eta' N)$ ,  $m_\pi \rightarrow m_{\eta'}$ .

Each vertex in (A2) is multiplied by a phenomenological cutoff function

$$F_B(p^2) = \frac{\Lambda_B^4}{(p^2 - m_B^2)^2 + \Lambda_B^4}, \quad B = N, N_{1/2}^*, \quad (A20)$$

where  $p^2$  denotes the four-momentum squared of off-shell baryon and  $\Lambda_B$  is the cutoff parameter. For spin-3/2 nucleon resonances the multi-dipole form factor is used and it is given by the following expression:

$$F_B(p^2) = \frac{\Lambda_B^4}{(p^2 - m_B^2)^2 + \Lambda_B^4} \left( \frac{m_B^2 \tilde{\Gamma}_B^2}{(p^2 - m_B^2)^2 + m_B^2 \tilde{\Gamma}_B^2} \right)^2, \quad B = N_{3/2}^*, \quad (A21)$$

with  $\tilde{\Gamma}_B = \Gamma_B / \sqrt{2^{1/3} - 1}$ ; see [89] where the spin-dependent hadronic form factor was introduced. In order to reduce the number of free parameters, for the cutoff parameters for spin-1/2 and spin-3/2 resonances,  $\Lambda_{N^*} = 1.2$  GeV is used, while  $\Lambda_N = 1.0$  GeV for the proton and neutron exchanges.

In considering of the nucleon and nucleon resonances in the  $s$  and  $u$  channels (see Fig. 10) some additional comments are in order. While the four-momenta squared of transferred  $s$ -channel baryons is  $p_s^2 = W_{\pi^- p}^2 > (m_N + m_\eta)^2 \gtrsim 2.21$  GeV $^2$ , this is not the case for transferred  $u$ -channel baryons where one has  $p_u^2 < (m_N - m_\eta)^2 \lesssim 0.15$  GeV $^2$ . The form factors (A20) and (A21) used to describe the  $p_{s,u}^2$  dependence of baryons are defined so that they reach unity if  $p_{s,u}^2 = m_B^2$ , i.e., the four-momentum squared is equal to the baryon mass squared  $m_B^2$ . These factors have a large impact on the cross section result, since  $\sigma_{\pi^- p \rightarrow \eta n}$  is proportional to  $(F_B(p^2))^4$ , and the exchanged baryons are relatively away from their mass shell ( $p^2 \neq m_B^2$ ). In practice, due to the form factors according to my parametrization, the  $N^*$  contributions in the  $u$  channel are largely suppressed. To be more precise, for the  $N(1535)$  contribution, the  $s$ -channel term gives  $\sigma = 3.184$  mb for  $W_{\pi^- p} = 1.53$  GeV and  $\sigma = 0.791$  mb for  $W_{\pi^- p} = 1.65$  GeV, while the  $u$ -channel term gives only  $\sigma = 0.062$   $\mu\text{b}$  and  $\sigma = 0.106$   $\mu\text{b}$ , respectively. For higher mass resonances,

there is also a similar order of magnitude difference between these two terms. This is the reason why the  $N^*$  exchanges in the  $u$  channel can be neglected. For the nucleon ( $N = n, p$ ) contributions, the situation is different, partly due to the form-factor functions, but also due to the smaller mass in the propagators. There, the  $s$ -channel term gives  $\sigma = 1.7$   $\mu\text{b}$  for  $W_{\pi^- p} = 1.53$  GeV and  $\sigma = 1.4$   $\mu\text{b}$  for  $W_{\pi^- p} = 1.65$  GeV, while the  $u$ -channel term gives greater contributions  $\sigma = 17.7$   $\mu\text{b}$  and  $\sigma = 33.9$   $\mu\text{b}$ , respectively. Adding coherently these two contributions, one finds  $\sigma = 12.5$   $\mu\text{b}$  for  $W_{\pi^- p} = 1.53$  GeV and  $\sigma = 31.6$   $\mu\text{b}$  for  $W_{\pi^- p} = 1.65$  GeV. Since these terms are of similar order and interfere destructively especially in the low energy region, they cannot be neglected. The  $u$ -channel proton-exchange contribution plays an important role mainly in the backward scattering region,  $\cos \theta \approx -1$  (see the upper right panel of Fig. 12).

In the present calculation, to estimate the potential role of  $N(1650)$ ,  $N(1710)$ , and other resonances, the values of  $g_{MNN^*}$  coupling constants are taken from Table II. Note that the branching ratios determine only the square of the corresponding coupling constants, thus their signs must be fixed from independent studies. For example, for this purpose, the parameters of [19] follow the predictions of [84] (see Table IV of [84]).

There are a few remarkable observations to the  $N\eta$  channel. Note that from the PDG [73] the  $N(1535) \rightarrow N\pi, N\eta$  branching ratios are  $\approx 0.42$  (see Table II). The following  $N^* \rightarrow N\eta$  branching ratios can also be found in [90]:  $0.41 \pm 0.04$  for  $N(1535)$ ,  $0.33 \pm 0.04$  for  $N(1650)$ ,  $0.18 \pm 0.10$  for  $N(1710)$ . In Table II of [19] (Table 1 of [91]) to estimate the  $g_{\eta NN^*}$  coupling constants for the  $N(1650)$  and  $N(1710)$  smaller values 0.03–0.1 (0.065) and 0.06 (0.062), respectively, were used. As a result, the predictions presented there for the above resonances may be underestimated.

Figures 11 and 12 shows the total and differential cross-sections, respectively, for the reaction  $\pi^- p \rightarrow \eta n$ . Theoretical results for two models 1 and 2 are presented. Model 1 uses the PS-type couplings (A5), (A6) for all  $N^*$  resonances. Model 2 is similar to model 1 with the difference that for model 2 the PV-type couplings (A7), (A8) are used for all even-parity resonances included in the calculation. In both cases, the values for  $g_{MNN^*}$  were taken from Table II with the upper values for the  $N(1710)$ . The experimental data are from [92–101] (detailed analysis of the data obtained before 1980 can be found in the review by Clajus and Nefkens [102] and they were also discussed in Sec. III C of [103]). It can be seen from Fig. 11 that the  $N(1535)$  resonance gives a major contribution to the  $\pi^- p \rightarrow \eta n$  reaction. Clearly, the complete result indicates a large interference effect between different contributions, for example between  $N(1535)$  and  $N(1650)$ . From the upper right panel of Fig. 12 one can see that angular distribution of the  $N(1535)$  contribution is flat. The  $N(1520)$  contribution is very small, but it interferes with other contribu-

tions and is therefore necessary to describe the shape of the angular distribution at low energies. The  $u$ -channel  $N$  contribution plays an important role at the backward angle  $\cos \theta \approx -1$ . Model results for this reaction around

$W = 1.6$  GeV indicate an important contribution from  $N(1710)$  (see also [104]). At higher energies, the reaction mechanism is still under discussion; see [20, 83, 103–108].

TABLE II. Coupling constants for the  $MNN^*$  ( $M = \pi, \eta, \eta'$ ) vertices obtained from (A7)–(A12). Shown are the hadronic Breit-Wigner parameters for nucleon resonances, and the branching ratios ( $\mathcal{B}$ ) for adopted values and in the brackets from the PDG [73]. The coupling constants  $g_{MNN^*}$  are dimensionless. The symbol “(–)” indicates the negative sign of the  $g_{\eta NN(1650)}$  coupling constant.

$N^* J^P$	Mass (MeV)	Width (MeV)	Decay channel	$\mathcal{B}$ (%) [PDG]	$g_{MNN^*}^2/4\pi$
$N(1520) 3/2^-$	1515	110	$\pi N$	65 [60 $\pm$ 5]	0.204
			$\eta N$	0.08 [0.08 $\pm$ 0.01]	3.945
			$\pi\pi N$	34.92 [30 $\pm$ 5]	
$N(1535) 1/2^-$	1530	150	$\pi N$	50 [42 $\pm$ 10]	0.040
			$\eta N$	42 [42.5 $\pm$ 12.5]	0.290
			$\pi\pi N$	8 [17.5 $\pm$ 13.5]	
$N(1650) 1/2^-$	1650	125	$\pi N$	60 [60 $\pm$ 10]	0.037
			$\eta N$	25 [25 $\pm$ 10]	(–) 0.076
			$\pi\pi N$	15 [39 $\pm$ 19]	
$N(1700) 3/2^-$	1720	200	$\pi N$	12 [12 $\pm$ 5]	0.021
			$\eta N$	2 [seen] <sup>a</sup>	0.916
			$\pi\pi N$	86 [> 89]	
$N(1710) 1/2^+$	1710	140	$\pi N$	12.5 – 20 [12.5 $\pm$ 7.5]	0.101 – 0.161
			$\eta N$	30 – 50 [30 $\pm$ 20]	2.021 – 3.368
			$\pi\pi N$	57.5 – 30 [31 $\pm$ 17]	
$N(1720) 3/2^+$	1720	250	$\pi N$	11 [11 $\pm$ 3]	0.002
			$\eta N$	3 [3 $\pm$ 2]	0.079
			$\pi\pi N$	86 [> 50]	
$N(1880) 1/2^+$	1880	300	$\pi N$	17 [17 $\pm$ 14]	0.198
			$\eta N$	28 [28 $\pm$ 27]	1.798
			$\pi\pi N$	55 [> 32]	
$N(1895) 1/2^-$	1900	120	$\pi N$	5 [10 $\pm$ 8]	0.0025
			$\eta N$	30 [30 $\pm$ 15]	0.058
			$\eta' N$	25 [25 $\pm$ 15]	0.510
			$\pi\pi N$	40 [45.5 $\pm$ 28.5]	
$N(1900) 3/2^+$	1920	200	$\pi N$	10.5 [10.5 $\pm$ 9.5]	0.001
			$\eta N$	8 [8 $\pm$ 6]	0.064
			$\eta' N$	6 [6 $\pm$ 2]	9.862
			$\pi\pi N$	75.5 [> 56]	
$N(2100) 1/2^+$	2100	260	$\pi N$	20 [20 $\pm$ 12]	0.138
			$\eta N$	25 [25 $\pm$ 20]	0.750
			$\eta' N$	8 [8 $\pm$ 3]	0.942
			$\pi\pi N$	47 [> 55]	

<sup>a</sup> Note that  $\mathcal{B}(N(1700) \rightarrow \eta N) = (1 \pm 1)\%$  from [90].

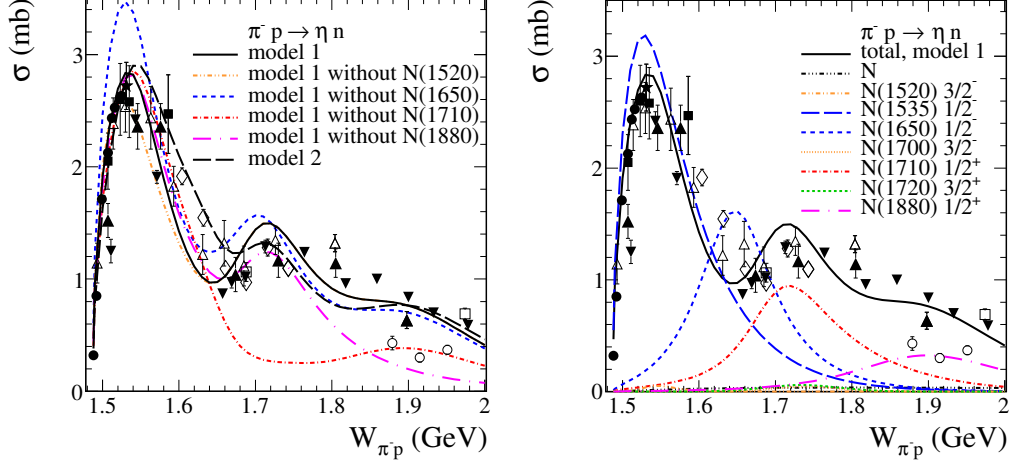


FIG. 11. Total cross section for the reaction  $\pi^- p \rightarrow \eta n$  as a function of the c.m. energy  $W_{\pi^- p}$ . Several  $N^*$  contributions, shown in the right panel, were included. The coherent sum of all contributions is shown by the solid and long-dashed lines, corresponding to model 1 and 2, respectively. Data are from [92] ( $\triangle$ ), [93] ( $\blacksquare$ ), [94] ( $\blacktriangle$ ), [95] ( $\square$ ), [96] ( $\star$ ), [97] ( $\diamond$ ), [99] ( $\blacktriangledown$ ), [100] ( $\circ$ ), [101] ( $\bullet$ ).

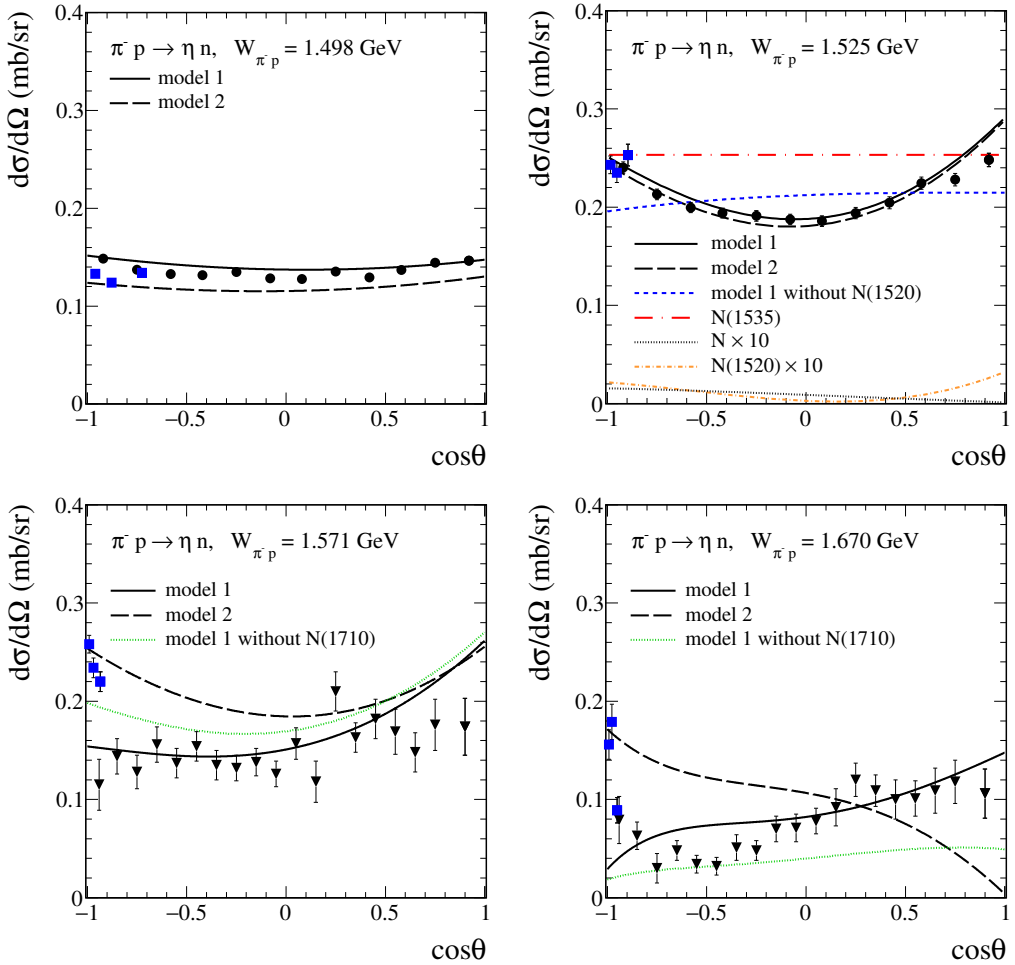


FIG. 12. The differential cross sections  $d\sigma/d\Omega$  for  $\pi^- p \rightarrow \eta n$  calculated for various  $W_{\pi p}$ . Data are from [101] ( $\bullet$ ), [99] ( $\blacktriangledown$ ), and in the backward scattering region from [98] ( $\blacksquare$ ). The solid and dashed lines represent the results for model 1 and model 2, respectively. In the right top panel, the  $N$  and  $N(1520)$  contributions multiplied by a factor 10 to be visible. In the bottom panels the green dotted lines correspond to the model without  $N(1710)$ .

## Appendix B: Photoproduction of the $\eta$ meson via reggeized-vector-meson exchanges

The unpolarized differential cross section for the  $\gamma p \rightarrow \eta p$  reaction is given by

$$\frac{d\sigma}{d\Omega} = \frac{1}{64\pi^2 s} \frac{|\mathbf{k}|}{|\mathbf{q}|} \frac{1}{4} \sum_{\text{spins}} |\mathcal{M}_{\gamma p \rightarrow \eta p}|^2, \\ d\Omega = \sin \theta d\theta d\phi. \quad (\text{B1})$$

The considerations are made in the center-of-mass (c.m.) frame,  $s$  is the invariant mass squared of the  $\gamma p$  system, and  $\mathbf{q}$  and  $\mathbf{k}$  are the c.m. three-momenta of the initial photon and final  $\eta$  meson, respectively. Taking the direction of  $\mathbf{q}$  as a  $z$  axis, the polar and azimuthal angles of  $\mathbf{k}$  are defined as  $\theta$  and  $\phi$ , respectively. The amplitude  $\mathcal{M}_{\gamma p \rightarrow \eta p}$  contains the processes shown in Fig. 13, that is, the  $s$ - and  $u$ -channel  $p$  and  $N^*$  exchanges and the  $t$ -channel vector-meson ( $V = \rho^0, \omega$ ) exchanges. In principle the contact-type interaction current that ensures gauge invariance should also be considered; see the discussion, e.g., in [109]. From a pragmatic point of view, however, only the tensor-type coupling in  $\gamma pp$  vertex is kept, while the vector-type coupling is omitted.

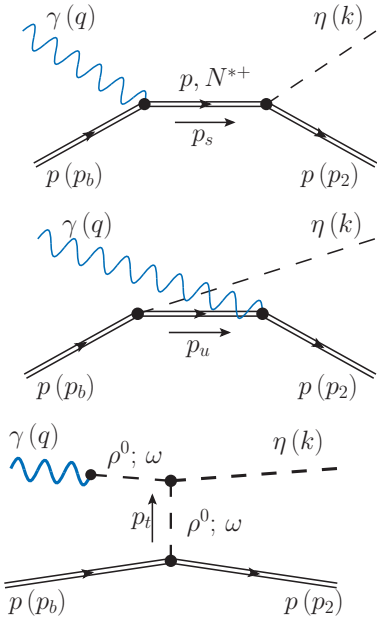


FIG. 13. Diagrams for photoproduction of the  $\eta$  meson.

The standard kinematic variables are

$$s = W_{\gamma p}^2 = (p_b + q)^2 = (p_2 + k)^2, \\ p_s = p_b + q = p_2 + k, \quad s = p_s^2, \\ p_u = p_b - k = p_2 - q, \quad u = p_u^2, \\ p_t = p_b - p_2 = k - q, \quad t = p_t^2. \quad (\text{B2})$$

The amplitude for the  $\gamma p \rightarrow \eta p$  reaction reads

$$\mathcal{M}_{\gamma p \rightarrow \eta p} = \mathcal{M}_s^{(p)} + \mathcal{M}_u^{(p)} + \sum_{N_{1/2}^*} \mathcal{M}_s^{(N_{1/2}^*)} + \sum_V \mathcal{M}_t^{(V)}. \quad (\text{B3})$$

It was checked numerically that the contributions from the  $u$ -channel  $N^*$  exchanges are small. The reason for this is explained in the previous section. Thus, these terms can be safely neglected in the considerations. Therefore, in the current analysis, only the  $s$ -channel  $N^*$  resonances with  $J^P = 1/2^\pm$  are considered. To calculate the amplitudes with the  $N^*$  and  $V$  (vector-meson) exchanges, the vector-meson-dominance (VMD) approach is used. Amplitudes with the virtual proton and  $N^*$  resonances are treated analogously as for the  $\pi^- p \rightarrow \eta n$  reaction discussed in Appendix A. Therefore, the focus will now be on the  $\eta$ -photoproduction process via the  $V$  exchanges.

The amplitude via the vector-meson exchanges includes two terms

$$\mathcal{M}_t^{(V)} = \mathcal{M}^{(\rho \text{ exchange})} + \mathcal{M}^{(\omega \text{ exchange})}. \quad (\text{B4})$$

The generic amplitude with  $V = \rho^0, \omega$ , for the diagram in Fig. 13, can be written as

$$\mathcal{M}^{(V \text{ exchange})} = (-i) \epsilon^{(\gamma) \mu''}(\lambda_\gamma) i \Gamma_{\mu'' \mu'}^{(\gamma \rightarrow V)}(q) i \Delta^{(V) \mu' \mu}(q) \\ \times i \Gamma_{\mu \nu}^{(VV\eta)}(q, p_t) i \tilde{\Delta}^{(V) \nu \nu'}(s, t) \\ \times \bar{u}(p_2, \lambda_2) i \Gamma_{\nu'}^{(Vpp)}(p_2, p_b) u(p_b, \lambda_b), \quad (\text{B5})$$

where  $p_b, p_2$  and  $\lambda_b, \lambda_2 = \pm \frac{1}{2}$  denote the four-momenta and helicities of the incoming and outgoing protons. In the equation above, reggeized treatment of  $\rho$  and  $\omega$  exchanges is used; see Eq. (2.23). For the building blocks of the amplitude (B5) see Sec. II. The VMD relations for the  $\gamma V$  transition vertices and  $\gamma_V$  couplings are given in Eqs. (3.23)–(3.25) of [36]. The above amplitude then can be expressed as follows:

$$\mathcal{M}^{(V \text{ exchange})} = \frac{e}{\gamma_V} \epsilon^{(\gamma) \mu}(\lambda_\gamma) \Gamma_{\mu \nu}^{(VV\eta)}(q, p_t) \tilde{\Delta}_T^{(V)}(s, t) \\ \times \bar{u}(p_2, \lambda_2) \Gamma^{(Vpp) \nu}(p_2, p_b) u(p_b, \lambda_b). \quad (\text{B6})$$

Here

$$\frac{4\pi}{\gamma_\rho^2} = 0.496 \pm 0.023, \quad \frac{4\pi}{\gamma_\omega^2} = 0.042 \pm 0.0015, \quad (\text{B7})$$

where  $\gamma_\rho > 0$  and  $\gamma_\omega > 0$ .

The  $g_{\omega\omega\eta}$  and  $g_{\rho\rho\eta}$  coupling constants occurring in the  $VV\eta$  vertices (2.16) were adjusted to the experimental decay widths  $\Gamma(\omega \rightarrow \eta\gamma)$  and  $\Gamma(\rho^0 \rightarrow \eta\gamma)$ , respectively. The amplitude for the reaction  $V(k_V, \epsilon^{(V)}) \rightarrow$

$\eta(k_\eta)\gamma(k_\gamma, \epsilon^{(\gamma)})$  is given by

$$\mathcal{M}^{(V \rightarrow \eta\gamma)} = -\frac{e}{\gamma_V} \frac{g_{VV\eta}}{2m_V} (\epsilon^{(\gamma)\mu}(\lambda_\gamma))^* \epsilon^{(V)\nu}(\lambda_V) \times \epsilon_{\mu\nu\alpha\beta} k_\gamma^\alpha k_V^\beta F^{(VV\eta)}(0, m_V^2, m_\eta^2), \quad (\text{B8})$$

where  $F^{(VV\eta)}(k_\gamma^2 = 0, k_V^2 = m_V^2, k_\eta^2 = m_\eta^2) = 1$ . In the calculations,  $\Gamma_\rho = 148$  MeV,  $m_\rho = 775$  MeV,  $\Gamma_\omega = 8.68$  MeV,  $m_\omega = 783$  MeV, and the central values of branching fractions  $\mathcal{B}(V \rightarrow \eta\gamma)$  are taken from the PDG [73]. Estimated values are  $|g_{\rho\eta\eta}| = 12.36$  and  $|g_{\omega\eta\eta}| = 12.16$ . It was assumed in the calculations that these coupling constants are positive.

The form factor in the  $VV\eta$  vertex  $i\Gamma_{\mu\nu}^{(VV\eta)}(q, p_t)$  in (B6) is

$$F^{(VV\eta)}(q^2, p_t^2, k^2) = F^{(VV\eta)}(0, p_t^2, m_\eta^2) = F_V(p_t^2) \quad (\text{B9})$$

and

$$F_V(t) = \frac{\Lambda_V^2 - m_V^2}{\Lambda_V^2 - t}. \quad (\text{B10})$$

From comparison of the model to the  $\eta$ -meson angular distributions from the CLAS experiment one can extract the cutoff parameter  $\Lambda_V = \Lambda_{V,\text{mon}}$ . Details will be given when discussing differential distributions below.

Figure 14 shows the integrated cross sections for the  $\gamma p \rightarrow \eta p$  reaction for two models, 1 and 2 (explained in the previous section), together with experimental data. It can be seen from the calculation results that the dominant production mechanism is via  $N(1535)$  resonance. At low energies, also the  $N(1650)$  play an important role, while at higher energies the  $N(1880)$  resonance is especially pronounced. From the top panel, one can see that the  $V$ -exchange contribution has different energy dependence of cross section and it plays some role rather at higher energies. There, the  $\rho$ -exchange term is much larger than the  $\omega$ -exchange term due to larger coupling constants both for the  $\gamma \rightarrow V$  transition vertex (B7) and for the tensor coupling in the  $V$ -proton vertex (2.19). There is a large interference between the two components.

Figure 15 shows the calculated results for the  $\gamma p \rightarrow \eta p$  reaction together with selected experimental data on  $d\sigma/d\cos\theta$  from [45–48]. The new CLAS data [48] are shown in the bottom panels, (c) – (e), as the black solid circles (●). They are consistent with earlier CLAS results [45] shown in the panel (b) but extend the energy range beyond the nucleon resonance region into the Regge regime, i.e. large  $W_{\gamma p}$  and  $\cos\theta$ . As illustrated in panel (c) for  $W_{\gamma p} \approx 2.38$  GeV and in the

very forward region the CBELSA/TAPS data [46] appear to be higher than the CLAS data [48]. The  $V$ -exchange contribution describes the new CLAS data [48] within their uncertainties only in the forward scattering region ( $0.5 < \cos\theta < 1.0$ ) and for  $W_{\gamma p} \gtrsim 2.4$  GeV.

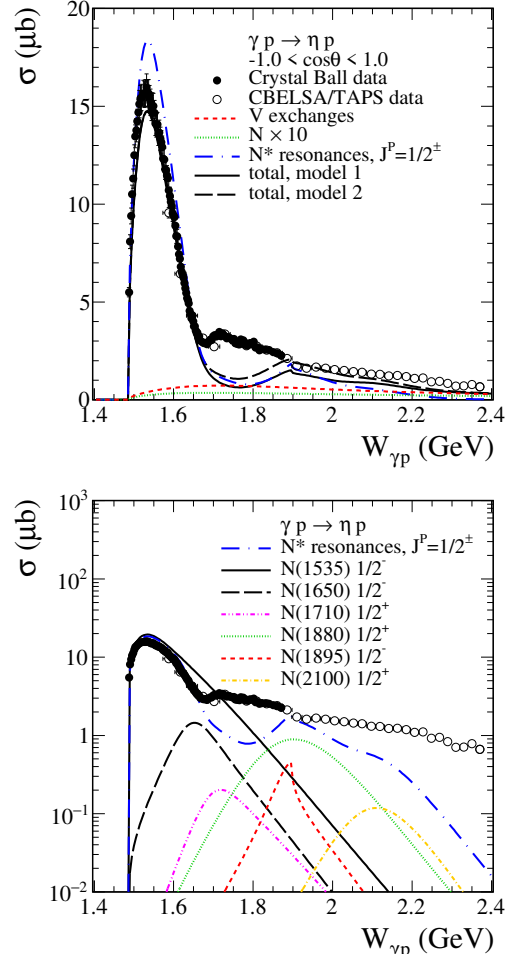


FIG. 14. The elastic  $\eta$  photoproduction cross section as a function of the center-of-mass energy  $W_{\gamma p}$  for  $-1.0 < \cos\theta < 1.0$ . The data from Crystal Ball (●) [47] and CBELSA/TAPS (○) [46] experiments are shown. Several contributions were included. The coherent sum of all contributions is shown by the solid and long-dashed lines, corresponding to model 1 and model 2, respectively. In the top panel, the  $N$  contribution is multiplied by a factor of 10 to make it visible. In the bottom panel, the  $N^*$  resonances included in the calculation are shown.

The reggeized-vector-meson-exchange model is not expected to describe the experimental data at lower energies. Indeed, this region is dominated by nucleon resonances; see Fig. 14 and the discussions in [20, 49]. It can be seen from Fig. 15 that with the increase of energy, the contributions of  $u$ -channel proton exchange and  $t$ -channel  $V$  exchange become more significant at the backward angle and forward angle respectively.

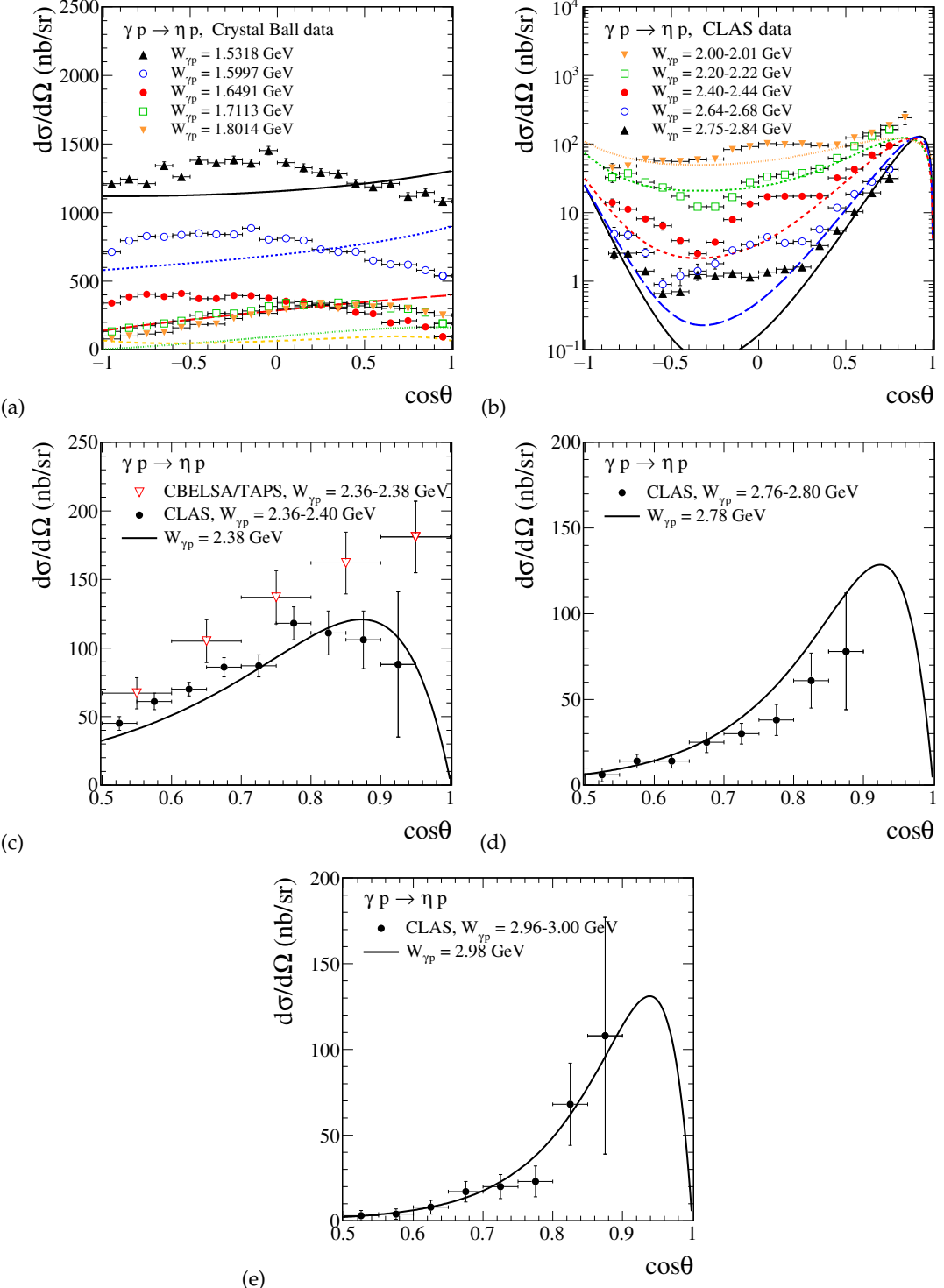


FIG. 15. The differential cross sections  $d\sigma/d\cos\theta$  for the  $\gamma p \rightarrow \eta p$  reaction. The curves represent the model results calculated for various  $W_{\gamma p}$  using  $\Lambda_{VNN} = 1.4$  GeV and  $\Lambda_{V,mon} = 1.2$  GeV. The Crystal Ball data in panel (a) are from [47]. The CLAS data on the panel (b) are taken from [45]. In panels (c), (d) and (e) the new CLAS data from [48] are presented; see the black solid circles (●) (these data points were scanned from Fig. 17 of [48]). In panel (c), data from the CBELSA/TAPS experiment [46] are shown for comparison.

Figure 16 shows a comparison of the theoretical results for  $d\sigma/dt$  with various experimental data, as described in the figure caption. Here, one deals with the kinematic region suited for the reggeized-vector-meson exchange

mechanism. It should be noted that the differential distribution at  $W_{\gamma p} = 2.38$  GeV peaks for  $\cos \theta = 0.88$  corresponding to  $-t = 0.23$  GeV $^2$ , while at  $W_{\gamma p} = 2.98$  GeV it peaks for  $\cos \theta = 0.94$  corresponding to  $-t = 0.20$  GeV $^2$  (see the right panel of Fig. 16). As a result of these comparisons, one can estimate the form factor in the  $VV\eta$  vertex, which describes the  $t$  dependencies of the  $V$  exchange. One finds the cutoff parameters  $\Lambda_{VNN} = 1.4$  GeV and  $\Lambda_{V,mon} = 1.3$  GeV with the same values for  $\rho^0$  and  $\omega$ .

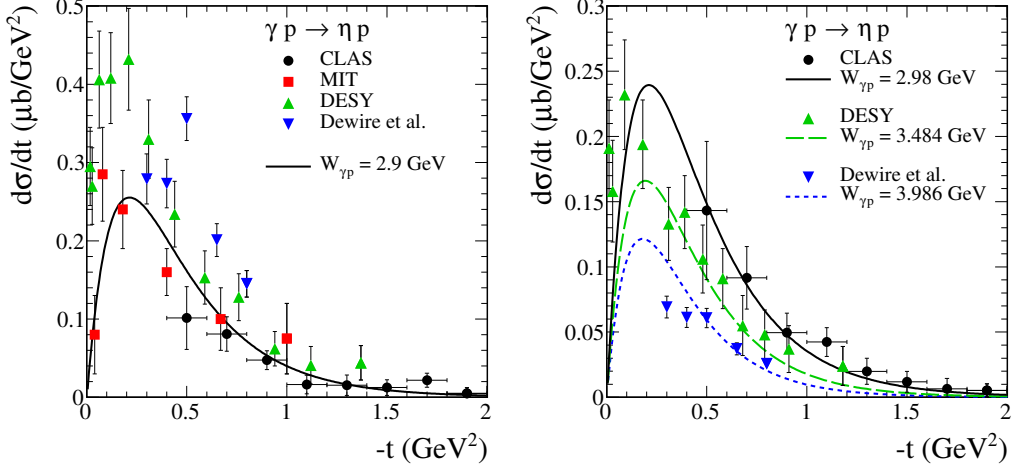


FIG. 16. The differential cross sections  $d\sigma/dt$  for the reaction  $\gamma p \rightarrow \eta p$ . The curves represent the model results calculated for various  $W_{\gamma p}$  using  $\Lambda_{VNN} = 1.4$  GeV and  $\Lambda_{V,mon} = 1.2$  GeV. Shown are data from CLAS [48] ( $\bullet$ ) (for  $W_{\gamma p} = 2.88 - 2.92$  and 2.98 GeV in the left and right panels, respectively), MIT [41] ( $\blacksquare$ ) (for  $W_{\gamma p} = 2.694 - 3.084$  GeV), DESY [42] ( $\blacktriangle$ ) (for  $W_{\gamma p} = 2.895$  and 3.484 GeV), and Dewire *et al.* [43] ( $\blacktriangledown$ ) (for  $W_{\gamma p} = 2.895$  and 3.986 GeV). The new CLAS data ( $\bullet$ ) were scanned from Fig. 18 of [48].

### Appendix C: The $N(1535) \rightarrow N\gamma$ and $N(1535) \rightarrow N\pi^+\pi^-$ decays and the $\rho NN(1535)$ coupling constant

In this Appendix, the  $\rho NN(1535)$  coupling constant is determined in two ways: one using the  $N(1535) \rightarrow N\rho^0 \rightarrow N\gamma$  decay, and the other using the  $N(1535) \rightarrow N\rho^0 \rightarrow N\pi^+\pi^-$  decay.

In the first method, the radiative decay of the  $N(1535)$

is considered as follows:

$$N(1535)(k_{N^*}, \lambda_{N^*}) \rightarrow N(k_N, \lambda_N) + \gamma(k_\gamma, \epsilon^{(\gamma)}), \quad (C1)$$

where  $k_N$ ,  $k_{N^*}$  and  $\lambda_N, \lambda_{N^*} = \pm 1/2$  denote the four-momenta and helicities of the nucleon and resonance, and  $k_\gamma$  and  $\epsilon^{(\gamma)}$  denote the four-momentum and polarization vector of photon with helicities  $\lambda_\gamma = \pm 1$ , respectively.

The amplitude for the reaction (C1) is given by

$$\begin{aligned} \mathcal{M}^{(N^* \rightarrow N\gamma)} &= (-i)\bar{u}(k_N, \lambda_N)i\Gamma_\mu^{(\rho NN^*)}(k_N, k_{N^*})u(k_{N^*}, \lambda_{N^*})i\Delta^{(\rho) \mu\nu}(k_\gamma)i\Gamma_{\nu k}^{(\rho \rightarrow \gamma)}(k_\gamma)(\epsilon^{(\gamma)\kappa}(\lambda_\gamma))^* \\ &= \frac{e}{\gamma_\rho}\bar{u}(k_N, \lambda_N)\Gamma_\mu^{(\rho NN^*)}(k_N, k_{N^*})u(k_{N^*}, \lambda_{N^*})(\epsilon^{(\gamma)\mu}(\lambda_\gamma))^*, \end{aligned} \quad (C2)$$

using the VMD ansatz for the coupling of the  $\rho^0$  meson to the photon; see (3.23)–(3.25) of [36]. The vertex for the  $\rho NN(1535)$  coupling can be derived from an effective coupling Lagrangian. However, different forms are commonly used in the literature. The gauge invariant

Lagrangian from (A6) of [20] is

$$\begin{aligned} \mathcal{L}_{\rho NN^*_{1/2^\mp}} &= -\frac{1}{2m_N}\bar{N}^*\begin{pmatrix} \gamma_5 \\ 1 \end{pmatrix} \left[ g_{\rho NN^*}^{(V)} \left( \frac{\gamma_\mu \partial^2}{m_{N^*} + m_N} - i\partial_\mu \right) \right. \\ &\quad \left. - g_{\rho NN^*}^{(T)} \sigma_{\mu\nu} \partial^\nu \right] (\boldsymbol{\tau} \boldsymbol{\Phi}_\rho^\mu) N + \text{h.c.}, \end{aligned} \quad (C3)$$

see Refs. [11, 12, 110], where the vector- and tensor-type

couplings were discussed. It is worth mentioning that a pure vector type of the form  $\propto \gamma_5 [\gamma_\mu \partial^\mu - (m_{N^*} + m_N) \partial_\mu]$  was derived in [111] and another variant of vector-type coupling in (23) of [112]. A pure tensor-type coupling was used, e.g., in [18, 19]. Note that the vector-type term of (C3) vanishes for the real photon in (C1), (C2) in the limit  $k_\gamma^2 = 0$ . The consideration here is limited to the pure tensor-type coupling of (C3) with  $g_{\rho NN^*} \equiv g_{\rho NN^*}^{(T)}$ .

In practical calculations, one introduces in the  $\Gamma_\mu^{(\rho NN^*)}$  vertex [derived from an effective coupling Lagrangian (C3)] the form factor

$$F_{\rho NN^*}(k_\rho^2, k_N^2, k_{N^*}^2) = \tilde{F}_\rho(k_\rho^2) F_B(k_N^2) F_B(k_{N^*}^2), \quad (C4)$$

with the assumption that  $\tilde{F}_\rho(k_\rho^2)$  is parametrized as

$$\tilde{F}_\rho(k_\rho^2) = \frac{\tilde{\Lambda}_\rho^4}{\tilde{\Lambda}_\rho^4 + (k_\rho^2 - m_\rho^2)^2}, \quad (C5)$$

where  $\tilde{\Lambda}_\rho$  is cutoff parameter. For the on shell case  $F_{\rho NN^*}(m_\rho^2, m_N^2, m_{N^*}^2) = 1$ . Then, for (C1) one has

$$\begin{aligned} F_{\rho NN^*}(k_\rho^2, k_N^2, k_{N^*}^2) &= F_{\rho NN^*}(0, m_N^2, m_{N^*}^2) \\ &= \tilde{F}_\rho(0) F_B(m_N^2) F_B(m_{N^*}^2) \\ &= \tilde{F}_\rho(0). \end{aligned} \quad (C6)$$

In the first method, the radiative decay width is,

$$\Gamma(N^* \rightarrow N\gamma)_{\text{tensor}} = \frac{e^2}{\gamma_\rho^2} \frac{g_{\rho NN^*}}{16\pi} \frac{k(m_N^2 - m_{N^*}^2)^2}{m_N^2 m_{N^*}^2} (\tilde{F}_\rho(0))^2. \quad (C7)$$

Here  $k$  is the photon momentum in the  $N^*$  rest frame,  $k = (m_{N^*}^2 - m_N^2)/2m_{N^*}$ . Then, the absolute value of coupling constant  $|g_{\rho NN^*}|$ , for  $i = 2$  or  $3$ , can be adjusted to the experimental radiative decay width:

$$\Gamma(N^* \rightarrow N\gamma) = \frac{k^2}{\pi} \frac{m_N}{m_{N^*}} |A_{1/2}|^2, \quad (C8)$$

where  $A_{1/2}$  represents the transverse helicity-1/2 amplitude for the proton,  $A_{1/2}^p = 0.105 \pm 0.015 \text{ GeV}^{-1/2}$  [73]. Note, that in Table III of [113] the value  $A_{1/2}^p = 0.107 \pm 0.003 \text{ GeV}^{-1/2}$  is given.

One can compare the results with those obtained using the experimental branching ratio for helicity 1/2 from the PDG compilation,  $\mathcal{B}(N(1535) \rightarrow p\gamma) = 0.15 - 0.30\%$  [73]. The value of the coupling constant  $|g_{\rho NN^*}|$  found in this way is smaller by a factor of 1.2 than that based on (C8).

In the second method, one considers the decay of  $N(1535)$  into a nucleon and two pions via an intermediate  $\rho$  meson, taking into account its mass distribution:

$$\begin{aligned} N(1535)(k_{N^*}, \lambda_{N^*}) \\ \rightarrow N(k_N, \lambda_N) + [\rho^0(k_\rho) \rightarrow \pi^+(k_1) + \pi^-(k_2)]. \end{aligned} \quad (C9)$$

The amplitude for the reaction (C9), denoted by  $\mathcal{M}^{(N^* \rightarrow N\pi^+\pi^-)}$ , is obtained from (C2) by making the replacement

$$\begin{aligned} i\Delta^{(\rho)\mu\nu}(k_\gamma) i\Gamma_{v\kappa}^{(\rho\rightarrow\gamma)}(k_\gamma) (\epsilon^{(\gamma)\kappa}(\lambda_\gamma))^* \\ \rightarrow i\Delta^{(\rho)\mu\nu}(k_\rho) i\Gamma_v^{(\rho\pi\pi)}(k_1, k_2) \\ = \frac{g_{\rho\pi\pi}}{2} \left( -g^{\mu\nu} + \frac{k_\rho^\mu k_\rho^\nu}{k_\rho^2} \right) \Delta_T^{(\rho)}(k_\rho^2) (k_1 - k_2)^\nu, \end{aligned} \quad (C10)$$

and taking

$$F_{\rho NN^*}(k_\rho^2, k_N^2, k_{N^*}^2) = F_{\rho NN^*}(k_\rho^2, m_N^2, m_{N^*}^2) = \tilde{F}_\rho(k_\rho^2) \quad (C11)$$

with  $k_\rho^2 = (k_1 + k_2)^2$ . The  $\rho^0$  propagator function and the  $\rho^0\pi^+\pi^-$  coupling in (C10) are taken from (4.1)–(4.6) and (3.35), (3.36) of [36], respectively.

For the decay process (C9) the phase-space integration can be evaluated numerically using the DECAY Monte Carlo generator [114]. The value of  $g_{\rho NN^*}$ , can be obtained from the experimental partial decay width  $\Gamma(N(1535) \rightarrow N\rho \rightarrow N\pi\pi)$ . Unfortunately, the branching ratio of the  $N(1535)$  state into the  $N\rho$  channel appears to be not well known in the literature. In [113] the following values were reported:  $\mathcal{B}(N(1535) \rightarrow N\rho) = 14 \pm 2\%$  and  $\mathcal{B}(N(1535) \rightarrow N\rho)_{\text{D-wave}} < 0.3\%$ . However, notably smaller value for the decay into S wave was found by the HADES Collaboration [115]  $\mathcal{B}(N(1535) \rightarrow N\rho) = 2.7 \pm 0.6\%$  and  $0.5 \pm 0.5\%$  for the decay into D wave. In the calculations, the value from [115] for the S wave was used.

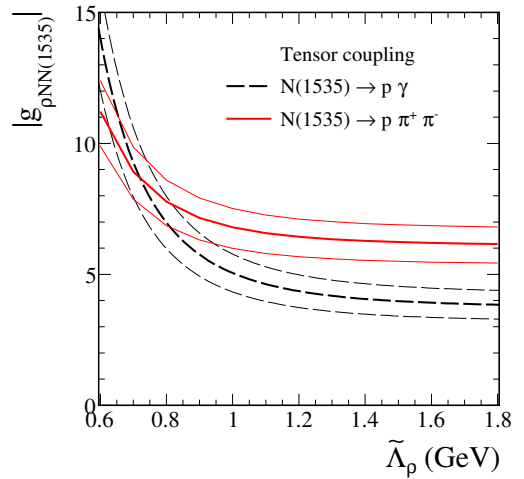


FIG. 17. Coupling constant constrained from the two decays  $N(1535)^+ \rightarrow p\gamma$  and  $N(1535)^+ \rightarrow p\pi^+\pi^-$  as a function of the cutoff parameter  $\tilde{\Lambda}_\rho$  in  $\tilde{F}_\rho$  (C5).

The results are shown in Fig. 17. From the radiative and two-pion decays of  $N(1535)$  resonance, one estimates the coupling constant  $g_{\rho NN^*} \equiv g_{\rho NN^*}^{(T)}$  occurring

in the vertex  $\Gamma_\mu^{(\rho NN^*)}$  (C3) versus the cutoff parameter  $\tilde{\Lambda}_\rho$  in  $\tilde{F}_\rho$  (C5). The values of coupling constants extracted from the available experimental data on the two decays are large. This implies that the  $\rho$ -exchange contribution may play an important role for the  $pp \rightarrow pp\eta$  process and should not be ignored. The thin upper and lower lines in Fig. 17 represent the results that comes from uncertainties in the input data used ( $A_{1/2}^p = 0.105 \pm 0.015 \text{ GeV}^{-1/2}$  [73],  $\mathcal{B}(N(1535) \rightarrow N\rho) = 2.7 \pm 0.6\%$  [115]).

Finally, Fig. 18 shows the numerical values of coupling constants  $\rho_{NN}(1650)$ ,  $\rho_{NN}(1710)$ ,  $\rho_{NN}(1880)$ ,  $\rho_{NN}(1895)$ , and  $\rho_{NN}(2100)$ , assuming the tensor-type coupling only, versus  $\tilde{\Lambda}_\rho$  estimated from (C7). For

$N(1650)$  one takes  $A_{1/2}^p = 0.045 \pm 0.010 \text{ GeV}^{-1/2}$  from [73], for  $N(1710)$  one takes  $A_{1/2}^p = 0.014 \pm 0.008 \text{ GeV}^{-1/2}$  [113], for  $N(1880)$  one takes  $A_{1/2}^p = 0.119 \pm 0.015 \text{ GeV}^{-1/2}$  [113], for  $N(1895)$  one takes  $A_{1/2}^p = 0.017 \pm 0.005 \text{ GeV}^{-1/2}$  [113], and for  $N(2100)$  one takes  $A_{1/2}^p = 0.032 \pm 0.014 \text{ GeV}^{-1/2}$  [113]. In the calculations of photon- and hadron-induced reactions the following values were used:  $g_{\rho NN}(1535) = 5.0$  or 4.5 (respectively, for model 1, 2, or 3),  $g_{\rho NN}(1650) = 1.5$ ,  $g_{\rho NN}(1710) = 0.4$ ,  $g_{\rho NN}(1880) = 1.5$ ,  $g_{\rho NN}(1895) = 0.5$ ,  $g_{\rho NN}(2100) = 0.5$ , and a universal value of  $\tilde{\Lambda}_\rho = 1.2 \text{ GeV}$  for all resonances.

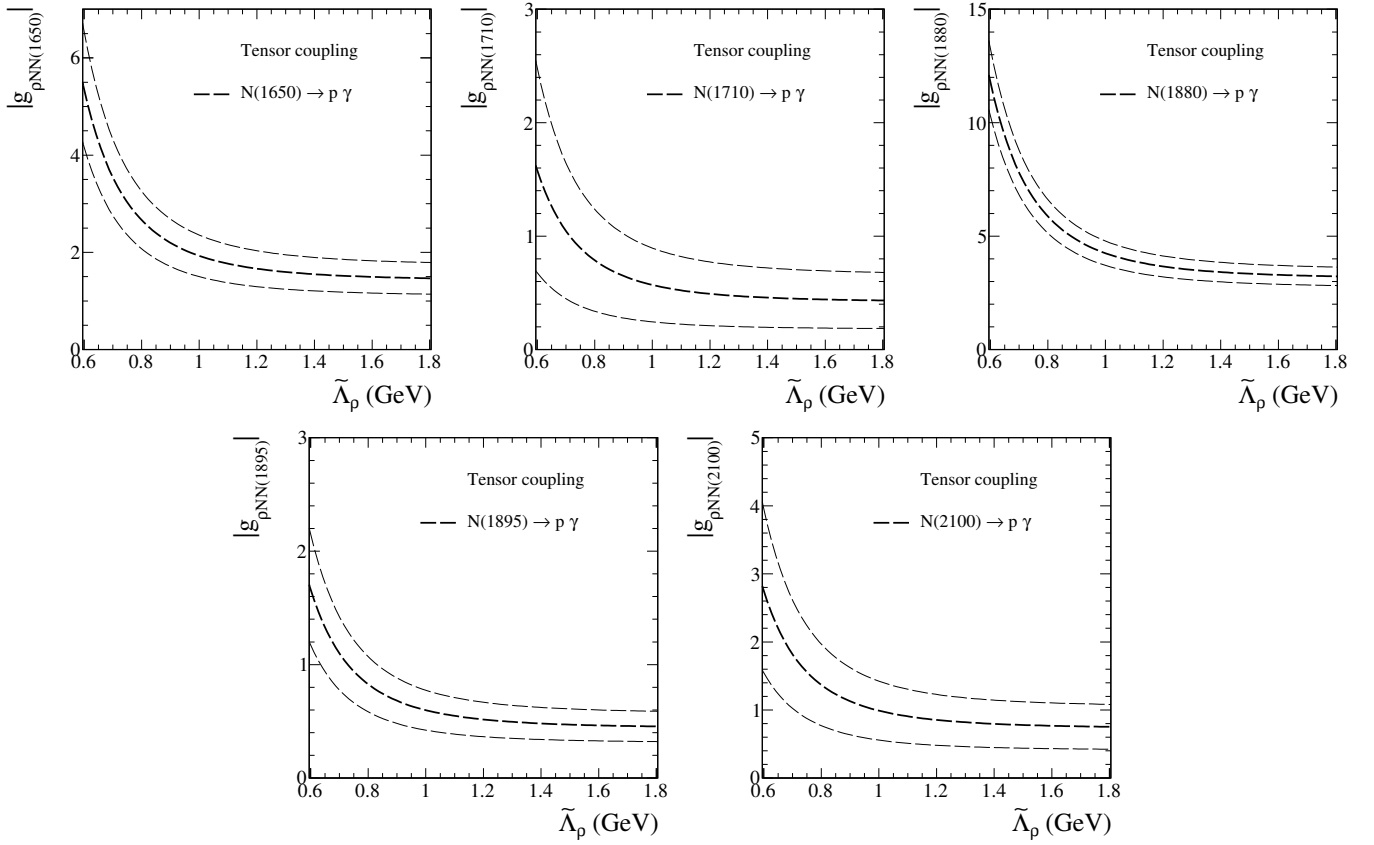


FIG. 18. Coupling constant constrained from the decays  $N(1650)^+, N(1710)^+, N(1880)^+, N(1895)^+, N(2100)^+ \rightarrow p\gamma$  as a function of  $\tilde{\Lambda}_\rho$ . The numerical results correspond to the tensor coupling case.

[1] L. Gan, B. Kubis, E. Passemard, and S. Tulin, *Precision tests of fundamental physics with  $\eta$  and  $\eta'$  mesons*, Phys. Rept. **945** (2022) 2191, arXiv:2007.00664 [hep-ph].

[2] J. F. Germond and C. Wilkin, *The  $pp \rightarrow pp\eta$  reaction near threshold*, Nucl. Phys. A **518** (1990) 308.  
[3] J. M. Laget, F. Wellers, and J. F. Lecolley,  *$\eta$ -meson*

production in nucleon-nucleon collisions, Phys. Lett. B **257** (1991) 254.

[4] T. Vetter, A. Engel, T. Biró, and U. Mosel,  $\eta$  production in nucleon-nucleon collisions, Phys. Lett. B **263** (1991) 153.

[5] M. Batinic, A. Svarc, and T. S. H. Lee, Near threshold  $\eta$  production in proton-proton collisions, Phys. Scripta **56** (1997) 321, arXiv:nucl-th/9604043.

[6] E. Gedalin, A. Moalem, and L. Razdolskaja, A covariant OBE model for  $\eta$  production in NN collisions, Nucl. Phys. A **634** (1998) 368, arXiv:hep-ph/9712375.

[7] A. B. Santra and B. K. Jain,  $\eta$  production in proton proton collisions, Nucl. Phys. A **634** (1998) 309.

[8] H. Calén *et al.*, Higher partial waves in  $pp \rightarrow pp\eta$  near threshold, Phys. Lett. B **458** (1999) 190, arXiv:nucl-ex/9811003.

[9] G. Fäldt and C. Wilkin, The production of  $\eta$  mesons in nucleon-nucleon collisions near threshold, Phys. Scripta **64** (2001) 427, arXiv:nucl-th/0104081.

[10] V. Baru, A. M. Gasparyan, J. Haidenbauer, C. Hanhart, A. E. Kudryavtsev, and J. Speth, Production of  $\eta$  mesons in nucleon-nucleon collisions, Phys. Rev. C **67** (2003) 024002, arXiv:nucl-th/0212014 [nucl-th].

[11] K. Nakayama, J. Speth, and T.-S. H. Lee,  $\eta$  meson production in NN collisions, Phys. Rev. C **65** (2002) 045210, arXiv:nucl-th/0202012 [nucl-th].

[12] K. Nakayama, J. Haidenbauer, C. Hanhart, and J. Speth, Analysis of the reaction  $pp \rightarrow pp\eta$  near threshold, Phys. Rev. C **68** (2003) 045201, arXiv:nucl-th/0302061.

[13] A. Fix and H. Arenhövel, Final state interaction in the reaction  $NN \rightarrow \eta NN$ , Phys. Rev. C **69** (2004) 014001, arXiv:nucl-th/0310034.

[14] A. Deloff, Phenomenology of  $pp \rightarrow pp\eta$  reaction close to threshold, Phys. Rev. C **69** (2004) 035206, arXiv:nucl-th/0309059.

[15] S. Ceci, A. Svarc, and B. Zauner, The importance of  $\eta$  exchange in the  $pp \rightarrow pp\eta$  process up to  $T_{lab} = 4.5$  GeV, Phys. Scripta **73** (2006) 663, arXiv:nucl-th/0402040.

[16] R. Czyzykiewicz *et al.*, Mechanism of Near-Threshold Production of the  $\eta$  Meson, Phys. Rev. Lett. **98** (2007) 122003, arXiv:hep-ex/0611015.

[17] P. Moskal *et al.*, Near threshold production of the  $\eta$  meson via the quasi-free  $pn \rightarrow pn\eta$  reaction, Phys. Rev. C **79** (2009) 015208, arXiv:0807.0722 [hep-ex].

[18] L. P. Kaptari and B. Kämpfer, Di-electrons from  $\eta$ -meson Dalitz decay in proton-proton collisions, Eur. Phys. J. A **33** (2007) 157, arXiv:nucl-th/0702033.

[19] R. Shyam,  $\eta$ -meson production in nucleon-nucleon collisions within an effective Lagrangian model, Phys. Rev. C **75** (2007) 055201, arXiv:nucl-th/0701011.

[20] K. Nakayama, Y. Oh, and H. Haberzettl, Combined Analysis of  $\eta$  Meson Hadro- and Photoproduction off Nucleons, J. Korean Phys. Soc. **59** (2011) 224, arXiv:0803.3169 [hep-ph].

[21] P. Klaja *et al.*, Measurement of the invariant mass distributions for the  $pp \rightarrow pp\eta'$  reaction at excess energy of  $Q = 16.4$  MeV, Phys. Lett. B **684** (2010) 11, arXiv:1001.5174 [nucl-ex].

[22] Q.-F. Lü and D.-M. Li, Near-threshold  $\eta$  production in  $pp$  collisions, Chin. Phys. C **39** no. 11, (2015) 113104, arXiv:1501.06266 [nucl-th].

[23] B. Krusche and C. Wilkin, Production of  $\eta$  and  $\eta'$  mesons on nucleons and nuclei, Prog. Part. Nucl. Phys. **80** (2015) 43, arXiv:1410.7680 [nucl-ex].

[24] F. Balestra *et al.*, (DISTO Collaboration), Exclusive  $\eta$  production in proton-proton reactions, Phys. Rev. C **69** (2004) 064003.

[25] K. Teilab, (HADES Collaboration),  $\omega$  and  $\eta$  meson production in  $p + p$  reactions at  $E_{kin} = 3.5$  GeV, Int. J. Mod. Phys. A **26** (2011) 694, arXiv:1009.3442 [nucl-ex].

[26] K. Teilab, The production of  $\eta$  and  $\omega$  mesons in 3.5 GeV  $p+p$  interaction in HADES, Ph.D. thesis, Frankfurt University, 2011, available at <https://hades.gsi.de/node/4>.

[27] G. Agakishiev *et al.*, (HADES Collaboration), Study of exclusive one-pion and one-eta production using hadron and dielectron channels in  $pp$  reactions at kinetic beam energies of 1.25 GeV and 2.2 GeV with HADES, Eur. Phys. J. A **48** (2012) 74, arXiv:1203.1333 [nucl-ex].

[28] S. Treliński, Exclusive production of  $\eta$  and  $\omega$  in  $pp$  at 4.5 GeV with HADES presented at Workshop at 1 GeV scale: From mesons to axions, September 19-20, 2024, Jagiellonian University, Kraków, Poland, available at <https://indico.meson.if.edu.pl/event/5/contributions/42>

[29] S. Treliński and I. Ciepał, Application of Kinematic Fit with Missing Particle Constraint in Proton-Proton Collisions with HADES, Acta Phys. Pol. B Proc. Suppl. **18** (2025) 4–A8.

[30] P. Lebiedowicz, O. Nachtmann, P. Salabura, and A. Szczurek, Exclusive  $f_1(1285)$  meson production for energy ranges available at the GSI-FAIR with HADES and PANDA, Phys. Rev. D **104** no. 3, (2021) 034031, arXiv:2105.07192 [hep-ph].

[31] QCD at FAIR Workshop 2024, <https://indico.gsi.de/event/20301/>.

[32] N. I. Kochelev, T. Morii, and A. V. Vinnikov, Pomeron fusion and central  $\eta$  and  $\eta'$  meson production, Phys. Lett. B **457** (1999) 202, arXiv:hep-ph/9903279 [hep-ph].

[33] N. I. Kochelev, T. Morii, B. L. Reznik, and A. V. Vinnikov, The role of secondary Reggeons in central meson production, Eur. Phys. J. A **8** (2000) 405, arXiv:hep-ph/0005088 [hep-ph].

[34] P. Lebiedowicz, O. Nachtmann, and A. Szczurek, Exclusive central diffractive production of scalar and pseudoscalar mesons; tensorial vs. vectorial pomeron, Annals Phys. **344** (2014) 301, arXiv:1309.3913 [hep-ph].

[35] P. Lebiedowicz, O. Nachtmann, and A. Szczurek, Central exclusive production of  $\eta$  and  $\eta'$  mesons in diffractive proton-proton collisions at the LHC within the tensor-pomeron approach, arXiv:2506.04846 [hep-ph].

[36] C. Ewerz, M. Maniatis, and O. Nachtmann, A Model for Soft High-Energy Scattering: Tensor Pomeron and Vector Odderon, Annals Phys. **342** (2014) 31, arXiv:1309.3478 [hep-ph].

[37] M. J. Anderson, S. K. Domokos, J. A. Harvey, and N. Mann, Central production of  $\eta$  and  $\eta'$  via double Pomeron exchange in the Sakai-Sugimoto model, Phys. Rev. D **90** no. 8, (2014) 086010, arXiv:1406.7010 [hep-ph].

[38] M. J. Anderson, S. Domokos, and N. Mann, Central production of  $\eta$  via double Pomeron exchange and double Reggeon exchange in the Sakai-Sugimoto model, Phys. Rev. D **96** no. 4, (2017) 046002, arXiv:1612.07457 [hep-ph].

[39] P. Kroll and K. Passek-Kumerički, Two-gluon components of the  $\eta$  and  $\eta'$  mesons to leading-twist accuracy, Phys. Rev. D **67** (2003) 054017,

arXiv:hep-ph/0210045 [hep-ph].

[40] S. D. Bass and P. Moskal,  $\eta'$  and  $\eta$  mesons with connection to anomalous glue, *Rev. Mod. Phys.* **91** no. 1, (2019) 015003, arXiv:1810.12290 [hep-ph].

[41] D. Bellenger, S. Deutsch, D. Luckey, L. S. Osborne, and R. Schwitters, Photoproduction of  $\eta^0$  Mesons at 4 GeV, *Phys. Rev. Lett.* **21** (1968) 1205.

[42] W. Braunschweig, W. Erlewein, H. Frese, K. Luebelsmeyer, H. Meyer-Wachsmuth, D. Schmitz, A. Schultz Von Dratzig, and G. Wessels, Single photoproduction of  $\eta$ -mesons on hydrogen in the forward direction at 4 and 6 GeV, *Phys. Lett. B* **33** (1970) 236.

[43] J. Dewire, B. Gittelman, R. Loe, E. C. Loh, D. J. Ritchie, and R. A. Lewis, Photoproduction of eta mesons from hydrogen, *Phys. Lett. B* **37** (1971) 326.

[44] M. Dugger *et al.*, (CLAS Collaboration),  $\eta$  Photoproduction on the Proton for Photon Energies from 0.75 to 1.95 GeV, *Phys. Rev. Lett.* **89** (2002) 222002. [Erratum: *Phys. Rev. Lett.* **89**, 249904 (2002)].

[45] M. Williams *et al.*, (CLAS Collaboration), Differential cross sections for the reactions  $\gamma p \rightarrow p\eta$  and  $\gamma p \rightarrow p\eta'$ , *Phys. Rev. C* **80** (2009) 045213, arXiv:0909.0616 [nucl-ex].

[46] V. Credé *et al.*, (CBELSA/TAPS Collaboration), Photoproduction of  $\eta$  and  $\eta'$  mesons off protons, *Phys. Rev. C* **80** (2009) 055202, arXiv:0909.1248 [nucl-ex].

[47] E. F. McNicoll *et al.*, (Crystal Ball Collaboration at MAMI), Experimental study of the  $\gamma p \rightarrow \eta p$  reaction with the Crystal Ball detector at the Mainz Microtron (MAMI-C), *Phys. Rev. C* **82** (2010) 035208, arXiv:1007.0777 [nucl-ex]. [Erratum: *Phys. Rev. C* **84**, 029901 (2011)].

[48] T. Hu *et al.*, (CLAS Collaboration), Photoproduction of  $\eta$  mesons off the proton for  $1.2 < E_\gamma < 4.7$  GeV using CLAS at Jefferson Laboratory, *Phys. Rev. C* **102** (2020) 065203, arXiv:2006.01361 [nucl-ex].

[49] W.-T. Chiang, S. N. Yang, L. Tiator, M. Vanderhaeghen, and D. Drechsel, Reggeized model for  $\eta$  and  $\eta'$  photoproduction, *Phys. Rev. C* **68** (2003) 045202, arXiv:nucl-th/0212106.

[50] X.-H. Zhong and Q. Zhao,  $\eta$  photoproduction on quasifree nucleons in the chiral quark model, *Phys. Rev. C* **84** (2011) 045207, arXiv:1106.2892 [nucl-th].

[51] J. Nys, V. Mathieu, C. Fernández-Ramírez, A. N. Hiller Blin, A. Jackura, M. Mikhasenko, A. Pilloni, A. P. Szczepaniak, G. Fox, and J. Ryckebusch, (JPAC Collaboration), Finite-energy sum rules in eta photoproduction off a nucleon, *Phys. Rev. D* **95** no. 3, (2017) 034014, arXiv:1611.04658 [hep-ph].

[52] V. L. Kashevarov, M. Ostrick, and L. Tiator, Regge phenomenology in  $\pi^0$  and  $\eta$  photoproduction, *Phys. Rev. C* **96** no. 3, (2017) 035207, arXiv:1706.07376 [hep-ph].

[53] L. Tiator, M. Gorchtein, V. L. Kashevarov, K. Nikonorov, M. Ostrick, M. Hadžimehmedović, R. Omerović, H. Osmanović, J. Stahov, and A. Švarc, Eta and etaprime photoproduction on the nucleon with the isobar model EtaMAID2018, *Eur. Phys. J. A* **54** no. 12, (2018) 210, arXiv:1807.04525 [nucl-th].

[54] A. Sibirtsev and W. Cassing,  $\eta'$  Production in proton-proton collisions near threshold, *Eur. Phys. J. A* **2** (1998) 333, arXiv:nucl-th/9806022.

[55] C. Hanhart and K. Nakayama, On the treatment of NN interaction effects in meson production in NN collisions, *Phys. Lett. B* **454** (1999) 176, arXiv:nucl-th/9809059 [nucl-th].

[56] K. Nakayama, A. Szczurek, C. Hanhart, J. Haidenbauer, and J. Speth, Production of  $\omega$  mesons in proton-proton collisions, *Phys. Rev. C* **57** (1998) 1580, arXiv:nucl-th/9802013.

[57] L. P. Kaptari and B. Kämpfer, Combined analysis of near-threshold production of  $\omega$  and  $\phi$  mesons in nucleon-nucleon collisions within an effective meson-nucleon model, *Eur. Phys. J. A* **23** (2005) 291, arXiv:nucl-th/0406077 [nucl-th].

[58] R. Shyam and H. Lenske, Reaction  $\bar{p}p \rightarrow \bar{\Lambda}_c^- \Lambda_c^+$  within an effective Lagrangian model, *Phys. Rev. D* **90** no. 1, (2014) 014017, arXiv:1406.7071 [hep-ph].

[59] R. Shyam, Charmed-baryon production in antiproton-proton collisions within an effective Lagrangian model, *Phys. Rev. D* **96** no. 11, (2017) 116019, arXiv:1712.00352 [hep-ph].

[60] K. Nakayama, H. F. Arellano, J. W. Durso, and J. Speth,  $\eta'$  meson production in proton-proton collisions, *Phys. Rev. C* **61** (2000) 024001, arXiv:nucl-th/9908077.

[61] R. Machleidt, K. Holinde, and C. Elster, The bonn meson-exchange model for the nucleon-nucleon interaction, *Phys. Rept.* **149** (1987) 1.

[62] M. M. Brisudová, L. Burakovsky, and J. T. Goldman, Effective functional form of Regge trajectories, *Phys. Rev. D* **61** (2000) 054013, arXiv:hep-ph/9906293.

[63] K. Nakayama, J. W. Durso, J. Haidenbauer, C. Hanhart, and J. Speth,  $\phi$ -meson production in proton-proton collisions, *Phys. Rev. C* **60** (1999) 055209, arXiv:nucl-th/9904040.

[64] Repository for publication-related High-Energy Physics data. <https://www.hepdata.net/>.

[65] A. Baldini, V. Flaminio, W. G. Moorhead, and D. R. O. Morrison, Total Cross-Sections for Reactions of High Energy Particles, vol. 12 of *Landolt-Börnstein - Group I: Nuclear and Particle Physics*. Springer-Verlag Berlin, 1988.

[66] E. Pickup, D. K. Robinson, and E. O. Salant, Three-Pion Mass Distributions and the  $\eta$  Meson, *Phys. Rev. Lett.* **8** (1962) 329.

[67] G. Alexander, O. Benary, G. Czapek, B. Haber, N. Kidron, B. Reuter, A. Shapira, E. Simopoulou, and G. Yekutieli, Proton-Proton Interactions at 5.5 GeV/c, *Phys. Rev.* **154** (1967) 1284.

[68] J. Le Guyader, M. Sené, J. Ginetet, D. Manesse, T. Ha Anh, and D. Vignaud, Experimental study of four-prong events in proton-proton interactions at 13.1 GeV/c, *Nucl. Phys. B* **35** (1971) 573.

[69] E. Chiavassa *et al.*,  $\eta$  meson production in  $pd$  and  $pp$  collisions, *Phys. Lett. B* **337** (1994) 192.

[70] H. Calén *et al.*, The  $pp \rightarrow pp\eta$  reaction near the kinematical threshold, *Phys. Lett. B* **366** (1996) 39.

[71] F. Hibou *et al.*, Comparison of  $\eta$  and  $\eta'$  production in the  $pp \rightarrow pp\eta(\eta')$  reactions near threshold, *Phys. Lett. B* **438** (1998) 41, arXiv:nucl-ex/9802002.

[72] P. Moskal *et al.*, Invariant-mass distributions for the  $pp \rightarrow pp\eta$  reaction at  $Q = 10$  MeV, *Eur. Phys. J. A* **43** (2010) 131, arXiv:0912.1592 [nucl-ex].

[73] S. Navas *et al.*, (Particle Data Group), Review of particle physics, *Phys. Rev. D* **110** no. 3, (2024) 030001.

[74] H. W. Atherton *et al.*, *The reaction  $\bar{p}p \rightarrow \bar{p}p\pi^+\pi^-\pi^0$  at 5.7 GeV/c and a  $p\omega^0$  ( $\bar{p}\omega^0$ ) enhancement at 1.81 GeV*, *Nuovo Cim. A* **30** (1975) 505.

[75] G. W. Van Apeldoorn *et al.*, *Final states with a neutral meson and a  $\pi^+\pi^-$  or  $\bar{p}p$  pair in  $\bar{p}p$  interactions at 7.2 GeV/c*, *Nucl. Phys. B* **133** (1978) 245.

[76] F. Balestra *et al.*, (DISTO Collaboration),  *$\phi$  and  $\omega$  meson production in  $pp$  reactions at  $p_{lab} = 3.67$  GeV/c*, *Phys. Rev. C* **63** (2001) 024004, arXiv:nucl-ex/0011009.

[77] M. Benmerrouche, N. C. Mukhopadhyay, and J. F. Zhang, *Effective Lagrangian approach to the theory of  $\eta$  photoproduction in the  $N^*(1535)$  region*, *Phys. Rev. D* **51** (1995) 3237, arXiv:hep-ph/9412248.

[78] R. Machleidt, *High-precision, charge-dependent Bonn nucleon-nucleon potential*, *Phys. Rev. C* **63** (2001) 024001, arXiv:nucl-th/0006014.

[79] C. Wang, J. Hu, Y. Zhang, and H. Shen, *The charge-dependent Bonn potentials with pseudovector pion-nucleon coupling*, *Chin. Phys. C* **43** no. 11, (2019) 114107, arXiv:1909.06013 [nucl-th].

[80] Y. Li, M. K. Liou, and W. M. Schreiber, *Proton-proton bremsstrahlung calculation: Studies of the off-shell proton electromagnetic vertex and of pseudoscalar vs pseudovector  $\pi N$  couplings*, *Phys. Rev. C* **57** (1998) 507.

[81] L. Tiator, C. Bennhold, and S. S. Kamalov, *The  $\eta NN$  coupling in eta photoproduction*, *Nucl. Phys. A* **580** (1994) 455, arXiv:nucl-th/9404013.

[82] M. Kirchbach and L. Tiator, *On the coupling of the  $\eta$  meson to the nucleon*, *Nucl. Phys. A* **604** (1996) 385, arXiv:nucl-th/9601002.

[83] Q.-F. Lü, X.-H. Liu, J.-J. Xie, and D.-M. Li, *The near threshold  $\pi^- p \rightarrow \eta n$  reaction in an effective Lagrangian approach*, *Mod. Phys. Lett. A* **29** (2014) 1450012, arXiv:1312.5803 [hep-ph].

[84] T. Feuster and U. Mosel, *Photon- and meson-induced reactions on the nucleon*, *Phys. Rev. C* **59** (1999) 460, arXiv:nucl-th/9803057.

[85] T. Feuster and U. Mosel, *Unitary model for meson-nucleon scattering*, *Phys. Rev. C* **58** (1998) 457, arXiv:nucl-th/9708051.

[86] D. Drechsel, O. Hanstein, S. S. Kamalov, and L. Tiator, *A unitary isobar model for pion phot- and electroproduction on the proton up to 1 GeV*, *Nucl. Phys. A* **645** (1999) 145, arXiv:nucl-th/9807001.

[87] R. Shyam,  *$pp \rightarrow pK^+\Lambda$  reaction in an effective Lagrangian model*, *Phys. Rev. C* **60** (1999) 055213, arXiv:nucl-th/9901038.

[88] K. Nakayama and H. Haberzettl, *Analyzing  $\eta'$  photoproduction data on the proton at energies of 1.5 – 2.3 GeV*, *Phys. Rev. C* **73** (2006) 045211, arXiv:nucl-th/0507044.

[89] T. Vrancx, L. De Cruz, J. Ryckebusch, and P. Vancreyveld, *Consistent interactions for high-spin fermion fields*, *Phys. Rev. C* **84** (2011) 045201, arXiv:1105.2688 [nucl-th].

[90] J. Müller *et al.*, (CBELSA/TAPS Collaboration), *New data on  $\vec{\gamma}\vec{p} \rightarrow \eta p$  with polarized photons and protons and their implications for  $N^* \rightarrow N\eta$  decays*, *Phys. Lett. B* **803** (2020) 135323, arXiv:1909.08464 [nucl-ex].

[91] Z. Ouyang, J.-J. Xie, B.-S. Zou, and H.-S. Xu, *Theoretical study on  $pp \rightarrow pn\pi^+$  reaction at medium energies*, *Int.J.Mod.Phys. E* **18** (2009) 281, arXiv:0902.1818 [nucl-th].

[92] F. Bulos *et al.*, *Charge Exchange and Production of  $\eta$  Mesons and Multiple Neutral Pions in  $\pi^- p$  Reactions between 654 and 1247 MeV/c*, *Phys. Rev. E* **187** (1969) 1827.

[93] W. Deinet, H. Mueller, D. Schmitt, H. M. Staudenmaier, S. Buniatov, and E. Zavattini, *Differential and total cross-sections for  $\pi^- + p \rightarrow \eta + n$  from 718 to 1050 MeV/c*, *Nucl. Phys. B* **11** (1969) 495.

[94] W. B. Richards *et al.*, *Production and neutral decay of the  $\eta$  meson in  $\pi^- p$  collisions*, *Phys. Rev. D* **1** (1970) 10.

[95] J. E. Nelson, *A high statistics study of the reaction  $\pi^- p \rightarrow \pi^0 n$  between 1.0 and 2.4 GeV/c*, Ph.D. thesis, California University - Berkeley, 1972, Report No. LBL-1019 (unpublished).

[96] J. Feltesse, R. Ayed, P. Bareyre, P. Borgeaud, M. David, J. Ernwein, Y. Lemoigne, and G. Villet, *The reaction  $\pi^- p \rightarrow \eta n$  up to  $p_\eta^* = 450$  MeV/c: experimental results and partial-wave analysis*, *Nucl. Phys. B* **93** (1975) 242.

[97] R. B. Chaffee, *A study of the reaction  $\pi^- p \rightarrow \eta n$  in the region of the  $N^*(1688)$* , Lawrence Berkeley Laboratory, 1975, Report No. LBL-1060 (unpublished), <https://www.osti.gov/servlets/purl/4237887/>.

[98] N. C. Debenham, D. M. Binnie, L. Camilleri, J. Carr, A. Duane, D. A. Garbutt, W. G. Jones, J. Keyne, I. Siotis, and J. G. McEwen, *Backward  $\pi^- p$  reactions between 0.6 and 1.0 GeV/c*, *Phys. Rev. D* **12** (1975) 2545.

[99] R. M. Brown *et al.*, *Differential cross sections for the reaction  $\pi^- p \rightarrow \eta n$  between 724 and 2723 MeV/c*, *Nucl. Phys. B* **153** (1979) 89.

[100] H. R. Crouch *et al.*, *Cross sections for  $\pi^- + p \rightarrow n + k\pi^0$  ( $k = 1$  to 5) and  $\pi^- + p \rightarrow n + \eta^0$  ( $\eta^0 \rightarrow 2\gamma$ ) for incident pion momenta between 1.3 and 3.8 GeV/c*, *Phys. Rev. D* **21** (1980) 3023.

[101] S. Prakhov *et al.*, (Crystal Ball Collaboration), *Measurement of  $\pi^- p \rightarrow \eta n$  from threshold to  $p_{\pi^-} = 747$  MeV/c*, *Phys. Rev. C* **72** (2005) 015203.

[102] M. Clajus and B. M. K. Nefkens, *The  $\pi^- + p \rightarrow \eta + n$  Data Base*,  *$\pi N$  Newsletter* **7** (1992) 76.

[103] J. Durand, B. Juliá-Dáaz, T.-S. H. Lee, B. Saghai, and T. Sato, *Coupled-channels study of the  $\pi^- p \rightarrow \eta n$  process*, *Phys. Rev. C* **78** (2008) 025204, arXiv:0804.3476 [nucl-th].

[104] M. Shrestha and D. M. M. Manley, *Partial-wave analysis of the  $\pi^- p \rightarrow \eta n$  and  $\pi^- p \rightarrow K^0 \Lambda$  reactions*, *Phys. Rev. C* **86** (2012) 045204, arXiv:1205.5294 [hep-ph].

[105] X.-H. Zhong, Q. Zhao, J. He, and B. Saghai, *Study of  $\pi^- p \rightarrow \eta n$  at low energies in a chiral constituent quark model*, *Phys. Rev. C* **76** (2007) 065205, arXiv:0706.3543 [nucl-th].

[106] J. He and B. Saghai, *Combined study of  $\gamma p \rightarrow \eta p$  and  $\pi^- p \rightarrow \eta n$  in a chiral constituent quark approach*, *Phys. Rev. C* **80** (2009) 015207, arXiv:0812.1617 [nucl-th].

[107] D. Rönchen, M. Doring, F. Huang, H. Haberzettl, J. Haidenbauer, C. Hanhart, S. Krewald, U. G. Meissner, and K. Nakayama, *Coupled-channel dynamics in the reactions  $\pi N \rightarrow \pi N, \eta N, K\Lambda, K\Sigma$* , *Eur. Phys. J. A* **49** (2013) 44, arXiv:1211.6998 [nucl-th].

[108] L.-Y. Xiao, F. Ouyang, K.-L. Wang, and X.-H. Zhong, *Combined analysis of the  $\pi^- p \rightarrow K^0 \Lambda, \eta n$  reactions in a chiral quark model*, *Phys. Rev. C* **94** no. 3, (2016) 035202, arXiv:1602.04455 [nucl-th].

[109] F. Huang, M. Doring, H. Haberzettl, J. Haidenbauer, C. Hanhart, S. Krewald, U. G. Meissner, and

K. Nakayama, *Pion photoproduction in a dynamical coupled-channels model*, Phys. Rev. C **85** (2012) 054003, arXiv:1110.3833 [nucl-th].

[110] J.-J. Xie, C. Wilkin, and B.-S. Zou, *Coupling constant for  $N^*(1535)N\rho$* , Phys. Rev. C **77** (2008) 058202, arXiv:0802.2802 [nucl-th].

[111] D. O. Riska and G. E. Brown, *Nucleon resonance transition couplings to vector mesons*, Nucl. Phys. A **679** (2001) 577, arXiv:nucl-th/0005049.

[112] M. T. Peña, H. Garcilazo, and D. O. Riska, *The reaction  $pp \rightarrow pp\eta$  and the eta-nucleon and nucleon-nucleon interactions*, Nucl. Phys. A **683** (2001) 322, arXiv:nucl-th/0006011.

[113] B. C. Hunt and D. M. Manley, *Updated determination of  $N^*$  resonance parameters using a unitary, multichannel formalism*, Phys. Rev. C **99** no. 5, (2019) 055205, arXiv:1810.13086 [nucl-ex].

[114] R. A. Kycia, P. Lebiedowicz, and A. Szczurek, *DECAY: A Monte Carlo Library for the Decay of a Particle with ROOT Compatibility*, Commun. Comput. Phys. **30** no. 3, (2021) 942, arXiv:2011.14750 [hep-ph].

[115] J. Adamczewski-Musch *et al.*, (HADES Collaboration), *Two-pion production in the second resonance region in  $\pi^- p$  collisions with the High-Acceptance Di-Electron Spectrometer (HADES)*, Phys. Rev. C **102** no. 2, (2020) 024001, arXiv:2004.08265 [nucl-ex].